An Earth-sized Planet on the Verge of Tidal Disruption

Fei Dai[1,2,3] , Andrew W. Howard[3] , Samuel Halverson[4] , Jaume Orell-Miquel[5] , Enric Pallé[5] , Howard Isaacson[6,7] ,
Benjamin Fulton[8] , Ellen M. Price[9,60] , Mykhaylo Plotnykov[10] , Leslie A. Rogers[11] , Diana Valencia[10] ,
Kimberly Paragas[2] , Michael Greklek-McKeon[2] , Jonathan Gomez Barrientos[2] , Heather A. Knutson[2] , Erik A. Petigura[12] ,
Lauren M. Weiss[13] , Rena Lee[1] , Casey L. Brinkman[1] , Daniel Huber[1,14] , Gumundur Stefánsson[15] , Kento Masuda[16] ,
Steven Giacalone[3] , Cicero X. Lu[17,61] , Edwin S. Kite[18] , Renyu Hu[19,20] , Eric Gaidos[21] , Michael Zhang[22] ,
Ryan A. Rubenzahl[3,62] , Joshua N. Winn[23] , Te Han[24] , Corey Beard[24,63] , Rae Holcomb[25] , Aaron Householder[26,27] ,
Gregory J. Gilbert[12] , Jack Lubin[12] , J. M. Joel Ong[1,64] , Alex S. Polanski[28] , Nicholas Saunders[1,62] , Judah Van Zandt[12] ,
Samuel W. Yee[29] , Jingwen Zhang[1,63] , Jon Zink[3] , Bradford Holden[30] , Ashley Baker[31] , Max Brodheim[32] ,
Ian J. M. Crossfield[33] , William Deich[30] , Jerry Edelstein[34] , Steven R. Gibson[31] , Grant M. Hill[32] , Sharon R Jelinsky[34] ,
Marc Kassis[32] , Russ R. Laher[8] , Kyle Lanclos[32] , Scott Lilley[32] , Joel N. Payne[32] , Kodi Rider[34] , Paul Robertson[25] ,
Arpita Roy[35] , Christian Schwab[36] , Abby P. Shaum[3] , Martin M. Sirk[34] , Chris Smith[34] , Adam Vandenberg[32] ,
Josh Walawender[32] , Sharon X. Wang[37] , Shin-Ywan (Cindy) Wang[8] , Edward Wishnow[34] , Jason T. Wright[38,39,40] ,
Sherry Yeh[32] , José A. Caballero[41] , Juan C. Morales[42,43] , Felipe Murgas[5,44] , Evangelos Nagel[45] , Ansgar Reiners[45] ,
Andreas Schweitzer[46] , Hugo M. Tabernero[47] , Mathias Zechmeister[45] , Alton Spencer[48] , David R. Ciardi[49] ,
Catherine A. Clark[4,49] , Michael B. Lund[49] , Douglas A. Caldwell[50] , Karen A. Collins[29] , Richard P. Schwarz[29] ,
Khalid Barkaoui[51,52,53] , Cristilyn Watkins[29] , Avi Shporer[54] , Norio Narita[5,55,56] , Akihiko Fukui[5,55] , Gregor Srdoc[57] ,
David W. Latham[29] , Jon M. Jenkins[58] , George R. Ricker[54] , Sara Seager[26,54,59] , and Roland Vanderspek[54]

[1] Institute for Astronomy, University of Hawaiʻi, 2680 Woodlawn Drive, Honolulu, HI 96822, USA; fdai@hawaii.edu
[2] Division of Geological and Planetary Sciences, 1200 E California Boulevard, Pasadena, CA 91125, USA
[3] Department of Astronomy, California Institute of Technology, Pasadena, CA 91125, USA
[4] Jet Propulsion Laboratory, California Institute of Technology, 4800 Oak Grove Drive, Pasadena, CA 91109, USA
[5] Instituto de Astrofísica de Canarias (IAC), Calle Vía Láctea s/n, 38205 La Laguna, Tenerife, Spain
[6] Department of Astronomy, University of California Berkeley, Berkeley, CA 94720, USA
[7] Centre for Astrophysics, University of Southern Queensland, Toowoomba, QLD 4350, Australia
[8] NASA Exoplanet Science Institute/Caltech-IPAC, MC 314-6, 1200 E California Boulevard, Pasadena, CA 91125, USA
[9] Department of the Geophysical Sciences, University of Chicago, 5734 South Ellis Avenue, Chicago, IL 60637, USA
[10] Centre for Planetary Sciences, University of Toronto, 1265 Military Trail, Toronto, ON, M1C 1A4, Canada
[11] Department of Astronomy and Astrophysics, University of Chicago, Chicago, IL 60637, USA
[12] Department of Physics & Astronomy, University of California Los Angeles, Los Angeles, CA 90095, USA
[13] Department of Physics and Astronomy, University of Notre Dame, Notre Dame, IN 46556, USA
[14] Sydney Institute for Astronomy (SIfA), School of Physics, University of Sydney, NSW 2006, Australia
[15] Anton Pannekoek Institute for Astronomy, University of Amsterdam, Science Park 904, 1098 XH Amsterdam, The Netherlands
[16] Department of Earth and Space Science, Osaka University, Osaka 560-0043, Japan
[17] Gemini Observatory/NSF's NOIRLab, 670 N. A'ohoku Place, Hilo, HI 96720, USA
[18] Department of Geophysical Sciences, University of Chicago, Chicago, IL 60637, USA
[19] Jet Propulsion Laboratory, California Institute of Technology, Pasadena, CA 91109, USA
[20] Division of Geological and Planetary Sciences, California Institute of Technology, Pasadena, CA 91125, USA
[21] Department of Earth Sciences, University of Hawai'i at Mänoa, 1680 East-West Road, Honolulu, HI 96822, USA
[22] Department of Astronomy & Astrophysics, University of Chicago, Chicago, IL 60637, USA
[23] Department of Astrophysical Sciences, Princeton University, 4 Ivy Lane, Princeton, NJ 08544, USA
[24] Department of Physics & Astronomy, The University of California, Irvine, Irvine, CA 92697, USA
[25] Department of Physics & Astronomy, University of California Irvine, Irvine, CA 92697, USA
[26] Department of Earth, Atmospheric and Planetary Sciences, Massachusetts Institute of Technology, Cambridge, MA 02139, USA
[27] Kavli Institute for Astrophysics and Space Research, Massachusetts Institute of Technology, Cambridge, MA 02139, USA
[28] Department of Physics and Astronomy, University of Kansas, Lawrence, KS 66045, USA
[29] Center for Astrophysics | Harvard & Smithsonian, 60 Garden Street, Cambridge, MA 02138, USA[60]
[30] University of California Observatories University of California, Santa Cruz 1156 High Street, Santa Cruz, CA 95064, USA
[31] Caltech Optical Observatories, Pasadena, CA, 91125, USA
[32] W. M. Keck Observatory, 65-1120 Mamalahoa Highway, Waimea, HI 96743, USA
[33] Department of Physics & Astronomy, University of Kansas, 1082 Malott, 1251 Wescoe Hall Drive, Lawrence, KS 66045, USA
[34] Space Sciences Laboratory, University of California Berkeley, Berkeley, CA 94720, USA
[35] Astrophysics & Space Institute, Schmidt Sciences, New York, NY 10011, USA
[36] School of Mathematical and Physical Sciences, Macquarie University, Balaclava Road, North Ryde, NSW 2109, Australia
[37] Department of Astronomy, Tsinghua University, Beijing 100084, People's Republic of China
[38] Department of Astronomy & Astrophysics, 525 Davey Laboratory, Penn State, University Park, PA 16802, USA
[39] Center for Exoplanets and Habitable Worlds, 525 Davey Laboratory, Penn State, University Park, PA 16802, USA
[40] Penn State Extraterrestrial Intelligence Center, 525 Davey Laboratory, Penn State, University Park, PA 16802, USA
[41] Centro de Astrobiología (CSIC-INTA), ESAC campus, Camino Bajo del Castillo s/n, 28692 Villanueva de la Cañada, Madrid, Spain
[42] Institut de Ciències de l'Espai (ICE, CSIC), Campus UAB, Can Magrans sn, 08193 Bellaterra, Barcelona, Spain
[43] Institut d'Estudis Espacials de Catalunya (IEEC), 08034 Barcelona, Spain
[44] Departamento de Astrofísica, Universidad de La Laguna (ULL), 38206 La Laguna, Tenerife, Spain
[45] Institut für Astrophysik und Geophysik, Georg-August-Universität Göttingen, Friedrich-Hund-Platz 1, 37077 Göttingen, Germany
[46] Hamburger Sternwarte, Gojenbergsweg 112, D-21029 Hamburg, Germany
[47] Departamento de Física de la Tierra y Astrofísica & IPARCOS-UCM (Instituto de Física de Partículas y del Cosmos de la UCM), Facultad de Ciencias Físicas,
Universidad Complutense de Madrid, 28040 Madrid, Spain
[48] Western Connecticut State University, Danbury, CT 06810, USA

[49] NASA Exoplanet Science Institute/Caltech-IPAC, 1200 E. California Boulevard, Pasadena, CA 91125, USA
[50] SETI Institute, Mountain View, CA 94043 USA/NASA Ames Research Center, Moffett Field, CA 94035 USA
[51] Astrobiology Research Unit, Université de Liège, 19C Allée du 6 Août, 4000 Liège, Belgium
[52] Department of Earth, Atmospheric and Planetary Science, Massachusetts Institute of Technology, 77 Massachusetts Avenue, Cambridge, MA 02139, USA
[53] Instituto de Astrofísica de Canarias (IAC), Calle Vía Láctea s/n, 38200, La Laguna, Tenerife, Spain
[54] Department of Physics and Kavli Institute for Astrophysics and Space Research, Massachusetts Institute of Technology, Cambridge, MA 02139, USA
[55] Komaba Institute for Science, The University of Tokyo, 3-8-1 Komaba, Meguro, Tokyo 153-8902, Japan
[56] Astrobiology Center, 2-21-1 Osawa, Mitaka, Tokyo 181-8588, Japan
[57] Kotizarovci Observatory, Sarsoni 90, 51216 Viskovo, Croatia
[58] NASA Ames Research Center, Moffett Field, CA 94035, USA
[59] Department of Aeronautics and Astronautics, MIT, 77 Massachusetts Avenue, Cambridge, MA 02139, USA

Abstract

TOI-6255 b (GJ 4256) is an Earth-sized planet ($1.079 \pm 0.065\ R_\oplus$) with an orbital period of only 5.7 hr. With the newly commissioned Keck Planet Finder and CARMENES spectrographs, we determine the planet's mass to be $1.44 \pm 0.14\ M_\oplus$. The planet is just outside the Roche limit, with $P_{\rm orb}/P_{\rm Roche} = 1.13 \pm 0.10$. The strong tidal force likely deforms the planet into a triaxial ellipsoid with a long axis that is $\sim$10% longer than the short axis. Assuming a reduced stellar tidal quality factor $Q'_\star \approx 10^7$, we predict that tidal orbital decay will cause TOI-6255 to reach the Roche limit in roughly 400 Myr. Such tidal disruptions may produce the possible signatures of planet engulfment that have been seen on stars with anomalously high refractory elemental abundances compared to their conatal binary companions. TOI-6255 b is also a favorable target for searching for star–planet magnetic interactions, which might cause interior melting and hasten orbital decay. TOI-6255 b is a top target (with an Emission Spectroscopy Metric of about 24) for phase-curve observations with the James Webb Space Telescope.

Unified Astronomy Thesaurus concepts: Exoplanet formation (492); Exoplanet evolution (491); Star-planet interactions (2177)

1. Introduction

The "ultra-short-period" (USP) planets are generally terrestrial planets ($R < 2\,R_\oplus$) that orbit their host stars in less than one day (Sanchis-Ojeda et al. 2014). More than a hundred USPs have been described in the literature. Their occurrence rate around Sun-like stars is about 0.5% (Sanchis-Ojeda et al. 2014). USPs provide favorable opportunities to study the composition of terrestrial planets (Winn et al. 2018). A true Earth analog on a yearly orbit induces a Doppler wobble of $9\,\mathrm{cm\,s^{-1}}$, which is beyond the capabilities of current-generation spectrographs. The same planet on a subday orbit would induce a Doppler wobble of a few meters per second, which is within the reach of current spectrographs. Moreover, the irradiation of a USP by its host star is more than a thousand times the Earth's insolation. There is both theoretical and empirical evidence that any primordial H/He atmosphere on these planets would have been eroded by intensive mass loss (Sanchis-Ojeda et al. 2014; Lundkvist et al. 2016; Lopez 2017). Thus, one can directly make use of the mass and radius measurements to probe the planet's interior composition. USP planets are also amenable to observations of thermal phase curves and secondary eclipses with the James Webb Space Telescope (JWST). The albedo, phase offset, day–night temperature contrast, and emission spectra might reveal the presence or lack of an outgassed secondary atmosphere. In the absence of an atmosphere, phase-curve observation may reveal the dominant surface mineralogy on these rocky planets (Hu et al. 2012; Demory et al. 2016; Kreidberg et al. 2019a; Whittaker et al. 2022; Zhang et al. 2024).

Several recent works have suggested that the photospheric composition of a star can be significantly altered by the engulfment of rocky planets and their refractory elements (Ramírez et al. 2015; Oh et al. 2018; Nagar et al. 2019; Galarza et al. 2021; Behmard et al. 2023; Liu et al. 2024). Specifically, there are examples of stars for which the refractory elemental abundances are enhanced by about 0.1 dex relative to a comoving and presumably conatal binary companion. The USPs are the natural candidates for the planets that are engulfed and produce such signatures. Tidal interactions with the host star gradually shrink the orbit of a USP, and eventually bring them within the tidal disruption limit (Rappaport et al. 2013). The resulting debris would fall onto the surface convective layer of the host star and alter the photospheric abundances. The strength of tidal interaction is steeply dependent on the orbital separation (Equation (13)); thus, only the shortest-period planets may be tidally disrupted or engulfed by the host star within the age of the Universe (Jia & Spruit 2017; Winn et al. 2018). In this work, we present the discovery of perhaps the most compelling planet that is doomed for engulfment. TOI-6255 b is an Earth-sized planet with an extraordinarily short orbital period of merely 5.7 hr. Tidal disruption could happen in the next 400 Myr if the host star has a reduced tidal quality factor $Q'_\star = 10^7$.

In Section 2, we characterize the host star TOI-6255 in detail. We measure the radius of TOI-6255 b in Section 3 using transits. We extract the mass of the planet from Doppler observations in Section 4. In Section 5, we discuss the composition, tidal decay, tidal distortion, and phase curve of TOI-6255 b, as well as the suspected star–planet magnetic interaction. Section 6 is a summary of the paper.

Table 1
Stellar Parameters of TOI-6255 (GJ 4256; Gliese & Jahreiß, 1991)

Parameters	Value and 68.3% Confidence Interval	Reference
TIC ID	261135533	A
R.A.	22:06:00.76	A
Decl.	+39:17:55.8	A
V (mag)	12.747 ± 0.052	A
K_s (mag)	8.071 ± 0.02	A
Effective Temperature T_{eff} (K)	3421 ± 70	B
Surface Gravity $\log g$ (cm s^{-2})	4.850 ± 0.044	B
Iron Abundance [Fe/H] (dex)	-0.14 ± 0.09	B
Stellar Mass $M_\star$ ($M_\odot$)	0.353 ± 0.015	B
Stellar Radius $R_\star$ ($R_\odot$)	0.370 ± 0.011	B
Stellar Density $\rho_\star$ (g cm^{-3})	9.8 ± 1.0	B
Limb Darkening q_1 (Kipping 2013)	0.50 ± 0.28	B
Limb Darkening q_2 (Kipping 2013)	0.35 ± 0.18	B
Parallax π (mas)	49.0544 ± 0.0236	C

Note. References: A—TICv8; B—this work; and C—Gaia Collaboration et al. (2018).

2. Host Star Properties

2.1. Spectroscopic Analysis

We obtained a high-resolution, high-signal-to-noise-ratio (S/N), iodine-free spectrum of TOI-6255 with the High Resolution Echelle Spectrometer on the 10 m Keck Telescope (Vogt et al. 2014). The observation was taken on UT 2023 November 26. We exposed for 900 s and reached an S/N of about 80 per reduced pixel near 550 nm. We utilized the SpecMatch-Emp pipeline (Yee et al. 2017) to extract the spectroscopic parameters (T_{eff} and [Fe/H]). In short, Spec-Match-Emp crossmatches the observed spectrum of a star with a library of hundreds of well-calibrated stellar spectra observed by the California Planet Search collaboration. This empirical approach circumvents many known systematic effects that plague the direct spectral modeling of low-mass stars. Some of these systematic effects include the poor definition of a continuum and an imperfect molecular line list. SpecMatch-Emp gives an effective temperature $T_{eff} = 3421 \pm 70$ K and a metallicity [Fe/H] = -0.14 ± 0.09.

We then included the Gaia parallax (49.0544 ± 0.0236 mas; Gaia Collaboration et al. 2022) in our analysis. One can obtain a direct constraint on the stellar radius using the Stefan–Boltzmann law. The effective temperature, the K-band magnitude (minimal extinction), and the parallax (distance) of a star together constrain its radius. We used the Python package Isoclassify (Huber et al. 2017) to carry out this calculation. We adopted the MESA Isochrones & Stellar Tracks (MIST; Choi et al. 2016). We used default settings recommended by Isoclassify. Table 1 summarizes the posterior distribution of the stellar parameters of TOI-6255. We note that the Isoclassify results do not include any systematic errors that may be present in different theoretical model grids. Tayar et al. (2022) estimated a ~2% error on T_{eff}, ~4% on $M_\star$, and ~5% on $R_\star$.

To check on the systematic errors in stellar parameters, we performed an independent analysis using the CARMENES template spectrum of TOI-6255 (see Section 4.2 for details of the CARMENES observations). In short, the CARMENES data were analyzed with the publicly available SteParSyn package (Tabernero et al. 2022), in combination with the procedures described in Schweitzer et al. (2019) and Cifuentes et al. (2020a). While Isoclassify uses the MIST models, the SteParSyn parameter determination used a synthetic model grid computed using BT-Settl (Allard 2014) models, as described in (Marfil et al. 2021). The Isoclassify and SteParSyn results agree well within 1σ: $T_{eff} = 3421 \pm 70$ K (Isoclassify) versus 3455 ± 70 K (SteParSyn); $\log g = 4.850 \pm 0.044$ versus 4.78 ± 0.05; [Fe/H] = -0.14 ± 0.09 versus -0.16 ± 0.06; $M_\star = 0.353 \pm 0.015 M_\odot$ versus $0.357 \pm 0.019 M_\odot$; and $R_\star = 0.370 \pm 0.011 R_\odot$ versus $0.361 \pm 0.015 R_\odot$. All these values are also consistent with previous determinations by Lépine et al. (2013) and Gaidos et al. (2014).

We also checked whether there is infrared excess due to the presence of a debris disk, using the stellar photosphere models with stellar parameters derived from the CARMENES spectrum of TOI-6255. We plotted the Two Micron All Sky Survey JHK_s bands and the Wide-field Infrared Survey Explorer (WISE) W1, W2, W3, and W4 photometry and found no evidence for infrared excess out to 22 μm against a BT-Settl model, in agreement with the results of Cifuentes et al. (2020b). However, the WISE bands are not sensitive to colder debris disks. Finally, with the K_s magnitude and the Gaia parallax as input, the widely used empirical relation by Mann et al. (2019) also gives a mass of $0.3591 \pm 0.0086 M_\odot$, which is consistent with Isoclassify within 1σ. We chose to use the Isoclassify results for further analysis.

2.2. Nearby Stellar Companion

We checked if TOI-6255 has a nearby stellar companion that may produce a false-positive transit signal. We observed TOI-6255 with Palomar/PHARO (Hayward et al. 2001) on UT 2023 June 30. No stellar companion was detected in the narrowband Brγ filter ($\lambda_o = 2.1686$ μm; $\Delta\lambda = 0.0326$ μm). Each dither position was observed three times, offset in position from one another by 0″.5 for a total of 15 frames; with an integration time of 5.7 s per frame, the total on-source time was 85.5 s. Figure A1 shows the resultant contrast limit as a function of angular separation.

Using Gaia DR3 data (Gaia Collaboration et al. 2022), no comoving companion was identified within a radius of 10′. The Gaia Renormalised Unit Weight Error (RUWE) can be considered as a reduced χ^2 of their single-star astrometric solution. TOI-6255 has a RUWE of 1.39, just below the threshold of 1.4, below which the astrometric solution is considered consistent with a single star. This is consistent with the previous high-resolution imaging survey for close companions performed by Cortés-Contreras et al. (2017).

The proper motion of TOI-6255 reported by Gaia does not match with any known comoving associations reported in Banyan-Σ (Gagné et al. 2018) and in Bouma et al. (2022). Using the framework of Bensby et al. (2014), TOI-6255 has about a 4% chance of being in the thick disk, based on its Galactic UVW velocity (U, V, $W = 32.0 \pm 1.0$, -15.0 ± 2.1, -27.2 ± 0.5 km s^{-1}) after correcting for the local standard of rest. In this calculation, we used the values $U_\odot$, $V_\odot$, $W_\odot = 10.0 \pm 1.0$, 11.0 ± 2.0, 7.0 ± 0.5 km s^{-1} from Bland-Hawthorn & Gerhard (2016).

2.3. Host Star Age

While many methods of estimating stellar ages do not apply to M dwarfs, gyrochronology (relating a declining rotation rate to increasing age through temperature-dependent relations) may still be applicable. No periodic signal is obvious in either a Lomb–Scargle periodogram (Lomb 1976; Scargle 1982) or an autocorrelation analysis (McQuillan et al. 2014) of TESS light curves of TOI-6255, probably because the rotation periods of middle-aged mid-type M dwarfs are longer than the TESS orbit (and light-curve systematics timescale) of 13.7 days. Each TESS sector is 27 days in duration, and only two sectors have been observed for TOI-6255. Therefore, measuring the stellar rotation of TOI-6255 using TESS data can be challenging. A periodogram of a light curve from the longer-duration WASP survey (Pollacco et al. 2006) contains two peaks, at ∼68 and 85 days: application of the Gaidos et al. (2023) gyrochronology to the former yields an age of 6 ± 2 Gyr, consistent with main-sequence status. However, we caution that this gyrochronology is poorly calibrated at the cool end, and stars like TOI-6255 near or at the fully convective boundary can have markedly different spindown rates (e.g., Chiti et al. 2024).

3. Photometric Observations

3.1. TESS Observations

TESS (Ricker et al. 2015) observed TOI-6255 during Sectors 16 and 56 in 2019 September and in 2022 September. We downloaded the 2 minutes cadence light curve produced by the TESS Science Processing Operations Center (SPOC, of the NASA Ames Research Center; Jenkins et al. 2016a). The data are available on the Mikulski Archive for Space Telescopes website[65] (MAST 2021). Our analysis made use of both the Presearch Data Conditioning Simple Aperture Photometry (PDC-SAP; Stumpe et al. 2014) light curve and the Simple Aperture Photometry (SAP; Twicken et al. 2010; Morris et al. 2020) light curve. The PDC-SAP light curve underwent more extensive systematic mitigation and is hence used for modeling the transit signal. On the other hand, the SAP light curve better preserves any long-term stellar variability, so it was used in our phase-curve analysis and for the measurement of the rotation period for the host star. We discarded all data points that had a nonzero Quality Flag.

3.2. Additional Transiting Planets?

The TESS SPOC (Jenkins et al. 2016b) initially detected the transit of TOI-6255.01 (as a 0.238 days planet). We searched for other transiting signals in the light curve. We first removed any stellar activity or instrumental variation by fitting a cubic spline in time of a width of 0.75 days. We searched the detrended light curve with our own Box-Least-Square code (Kovács et al. 2002) that has been used in previous works (e.g., Dai et al. 2021). We recovered TOI-6255.01, as well as another 14.48 days transit-like signal, TOI-6255.02, with a signal detection efficiency (defined by Ofir 2014) of 14.3. This signal was independently reported on the ExoFOP website[66] by citizen scientist Alton Spencer. SPOC analysis of TOI-6255.02 showed a substantial flux centroid shift of $27'' \pm 3''$ toward a nearby background star. This suggests that TOI-6255.02 is

most likely a false positive. We are unable to detect any other prominent transit signal from the current data set.

3.3. Transit Modeling

Our transit model is based on the Python package Batman (Kreidberg 2015). The stellar density of the host star is a parameter for which a prior can be set by our spectroscopic analysis $\rho = 9.8 \pm 1.0$ g cm^{-3}. The stellar density is crucial for breaking the degeneracy between the semimajor axis and the impact parameter of the planet (Seager & Mallén-Ornelas 2003). For limb-darkening coefficients, we adopted the formulation of Kipping (2013; q_1 and q_2). The transit parameters further include the orbital period P_{orb}, the time of conjunction T_c, the planet-to-star radius ratio $R_p/R_\star$, the scaled orbital distance $a/R_\star$, the cosine of the orbital inclination $\cos i$, the orbital eccentricity e, and the argument of pericenter ω. e and ω are recombined to $\sqrt{e} \cos\omega$ and $\sqrt{e} \sin\omega$ to give rise to a uniform prior on eccentricity (Lucy & Sweeney 1971). We initially allowed for nonzero eccentricities. However, the resultant constraint on eccentricities using the current data set is weak (even after incorporating the radial velocity, or RV, data in Section 4.3). To reduce model complexity, we adopted circular orbits.

We first fitted all transits observed by TESS assuming a linear ephemeris (i.e., a constant period and no transit timing variations). The best-fit constant-period model was found by maximizing the likelihood with the Levenberg-Marquardt method implemented in the Python package lmfit (Newville et al. 2014). The best-fit constant-period model then served as a template model. Each individual transit was fitted with this template model. The only free parameters are the mid-transit times and three parameters for a quadratic function of time for any out-of-transit flux variation. This process yielded a list of individual transit times. We were not able to identify any statistically meaningful transit timing variations. To sample the posterior distribution of the transit parameters, we performed a Markov Chain Monte Carlo (MCMC) analysis using the emcee package (Foreman-Mackey et al. 2013). We initialized 128 walkers in the vicinity of the maximum-likelihood model from lmfit. We ran emcee for 50,000 steps, which is much longer than the autocorrelation length of each parameter (hundreds of steps). We summarize the posterior distribution in Table 2. Figure 1 is the phase-folded and binned transit of TOI-6255 b. TOI-6255 b has been confirmed by our strong RV detection and the well-modeled transit light curve (Section 4.3). Appendix B shows a tentative detection of phase-curve variation of TOI-6255 b in the TESS light curves. Appendix C shows additional transit modeling results using ground-based light curves.

4. Spectroscopic Observations

4.1. Keck Planet Finder Observations

The Keck Planet Finder (KPF; PI: A. Howard; Gibson et al. 2016, 2018, 2020) is an echelle spectrometer that was commissioned at the Keck Observatory in 2023 March. KPF covers the wavelength range of 445–870 nm with a resolving power of 98,000. Moreover, KPF's unique combination of high efficiency, 10 m aperture, and scheduling flexibility makes it well suited for studying USP planets. This paper is one of the first science results based on KPF data.

We observed TOI-6255 with KPF from 2023 May 22 to November 24, for a total of 91 exposures. The exposure time

Table 2
Planetary Parameters of TOI-6255

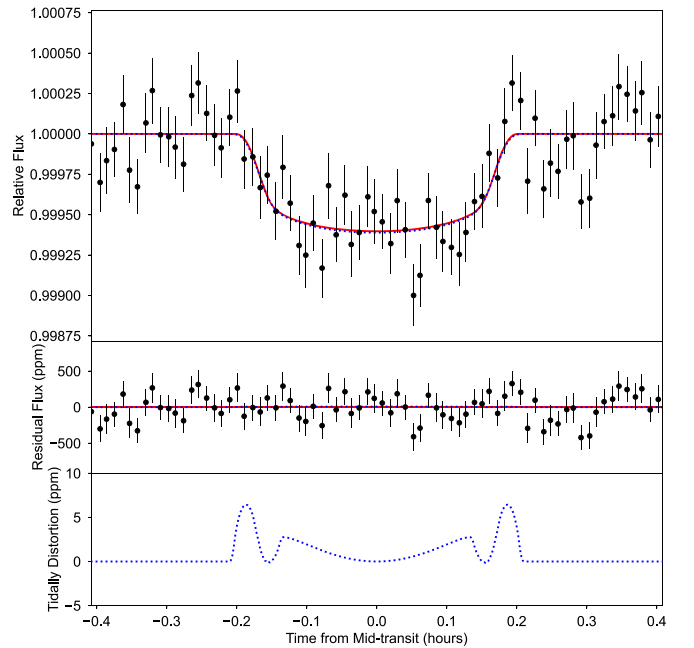| Parameter	Symbol	Posterior Distribution
TOI-6255 b		
Planet/Star Radius Ratio	$R_p/R_\star$	0.0267 ± 0.0014
Time of Conjunction (BJD 2457000)	T_c	1738.71248 ± 0.00043
Impact Parameter	b	0.84 ± 0.05
Scaled Semimajor Axis	$a/R_\star$	3.10 ± 0.12
Orbital Inclination (deg)	i	74.4 ± 1.2
Orbital Eccentricity	e	0 (fixed)
Orbital Period (days)	P_{orb}	$0.23818244 \pm 0.00000012$
RV Semi-amplitude (m s^{-1})	K	2.98 ± 0.28
Planetary Radius ($R_\oplus$)	R_p	1.079 ± 0.065
Planetary Mass ($M_\oplus$)	M_p	1.44 ± 0.14
KPF RV Jitter (m s^{-1})	σ_{KPF}	0.7 ± 0.3
CARMENES RV Jitter (m s^{-1})	$\sigma_{CARMENES}$	<0.4 (95% confidence)
Kernel Amplitude (m s^{-1})	h	8.9 ± 1.1
Correlation Timescale (days)	τ	$1.2^{+0.4}_{-0.1}$

Figure 1. Top: the transit of TOI-6255 b as observed by TESS. The black error bars are the phase-folded and binned TESS light curve. The red curve is our best-fit transit model. The blue dotted line also includes the effect of tidal distortion. Middle: the residual flux after removing the best-fit spherical planet model. Bottom: the correction due to tidal distortion amounts to no more than 10 ppm for TOI-6255 b. This is much smaller than the TESS photometric precision and remains unconstrained.

was 10 minutes. We achieved a typical S/N of 87 at 550 nm. The spectra were reduced with the KPF Data Reduction Pipeline (DRP), which is publicly available on Github.[67] The KPF DRP performs quadrant stitching, flat-fielding, order tracing, and optimal extraction. The host star is an M dwarf, for which traditional cross-correlation-function RV extraction is sometimes inferior to template-matching methods. The cross-correlation method is limited by the lack of a good line list for the many molecular absorption features that characterize the spectra of low-mass stars. The continuum level and a list of isolated lines are also hard to define. We used the publicly available template-matching code `serval` (Zechmeister et al. 2018) pipeline to extract the RVs from our KPF spectra.

KPF's wavelength calibration sources include Th–Ar and U–Ne lamps, a Laser Frequency Comb, a Fabry–Pérot Etalon, and the Solar Calibrator (Rubenzahl et al. 2023). The wavelength calibration sources and the wavelength calibration algorithm in the KPF DRP are still subject to fine-tuning at the time of writing this paper. Some of the apparent RV variations in our data for TOI-6255 are due to night-to-night instrumental drifts. Whenever possible, we tried to obtain several exposures of the star per calendar night, such that night-to-night instrumental drifts can be successfully mitigated, either with a correlated noise model or a floating chunk offset technique (see Section 4.3). Such an observational strategy has proven useful in the RV characterization of many USP planets (e.g., Howard et al. 2013). We implemented this observation strategy using the KPF Community Cadence algorithm described in Handley et al. (2024). The KPF RVs are shown in Tables 3 and 4.

4.2. CARMENES Observations

TOI-6255 was also observed with CARMENES (the Calar Alto high-Resolution search for M dwarfs with Exoearths with Near-infrared and optical Échelle Spectrographs; Quirrenbach et al. 2014, 2020), located at the 3.5 m telescope of the Calar Alto Observatory, Almería, Spain. CARMENES is a dual-channel spectrograph: the optical channel (VIS) covers the wavelength range from 0.52 to 0.96 μm ($\mathcal{R} = 94,600$), and the

near-infrared channel (NIR) covers from 0.96 to 1.71 μm ($\mathcal{R} = 80,400$).

We obtained 33 high-resolution spectra between 2023 June 24 and August 8. The exposure time was 30 minutes, and the typical median S/N achieved in the visible channel was about 68. The spectra were reduced using the `caracal` (Caballero et al. 2016) pipeline. We corrected the spectra for telluric absorption (Nagel et al. 2023) and derived relative RVs with the `serval` pipeline (Zechmeister et al. 2018). The RVs were further adjusted using measured nightly zero-point corrections (Trifonov et al. 2020). The CARMENES RVs are shown in Table 5.

4.3. Gaussian Process Model

The measured RV variations of TOI-6255 (Figure 2) display a correlated noise component that does not phase up with the orbital period of TOI-6255 b. As mentioned in Section 4.1, the correlated noise could be due to a combination of stellar activity and instrumental drifts. We employed a Gaussian Process (GP) model (e.g., Haywood et al. 2014; Grunblatt et al. 2015) to disentangle the planetary signals from the correlated noise component.

We used the same GP framework as in our previous works (Dai et al. 2019, 2021). However, instead of using a quasiperiodic kernel, which is widely used in exoplanet RV analyses (e.g., Haywood et al. 2014; Grunblatt et al. 2015), we used a simpler squared-exponential kernel. In other words, we dropped the periodic component of the quasiperiodic kernel. The quasiperiodic kernel is designed to model the quasiperiodic variation of stellar activity produced by the host star rotation coupled with its surface magnetic features. For TOI-6255, we were not able to robustly identify the quasiperiodic rotational modulation of TOI-6255 with TESS observations (Section 3).

Table 3
Keck/KPF RVs of TOI-6255

Time (BJD)	RV (m s^{-1})	RV Unc. (m s^{-1})
2460087.06212686	7.91	0.95
2460090.08283583	2.73	0.91
2460091.04582747	−5.73	0.84
2460093.05386041	−11.03	1.06
2460093.11093392	−12.58	1.05
2460100.02074132	−10.36	1.00
2460100.07705751	−4.79	1.12
2460100.98823238	−2.14	0.95
2460101.02651958	−0.00	0.87
2460106.06587267	−16.29	0.89
2460106.10595727	−18.94	0.91
2460124.04069331	−11.19	0.89
2460124.11356605	−6.04	0.96
2460126.07766735	9.79	1.03
2460126.11463478	6.95	0.89
2460129.99777854	−9.10	0.97
2460130.99139985	−5.80	1.00
2460135.10930206	−0.66	1.01
2460136.98291478	−8.14	1.49
2460137.07709318	−11.15	1.21
2460146.02819387	−1.36	1.02
2460146.10394072	−3.63	0.98
2460150.02103948	15.30	0.86
2460150.09242876	21.43	1.00
2460153.01666907	13.54	1.06
2460153.06132063	10.06	0.93
2460154.90337595	14.78	1.00
2460155.91078596	3.31	0.94
2460157.02830366	−1.22	0.96
2460157.05650057	−2.94	0.94
2460157.06840406	−2.94	0.98
2460185.76215501	−7.86	1.41
2460185.91568898	−8.41	1.46
2460186.05100537	−6.90	1.41
2460187.84396189	−10.25	1.01
2460188.00378558	−2.40	1.01
2460188.10885611	−7.88	1.29
2460188.77511581	−6.39	0.93
2460188.86314294	−1.67	0.96
2460188.96253992	2.61	1.08
2460190.00555127	1.58	0.92
2460190.04392353	4.74	1.00
2460190.07231719	7.42	1.04
2460191.00661120	5.15	1.00
2460191.05434485	10.08	0.92
2460191.07363138	14.80	0.81

Table 4
Table 3 Continued

Time (BJD)	RV (m s^{-1})	RV Unc. (m s^{-1})
2460192.02226241	15.08	0.92
2460192.03837202	14.70	0.92
2460192.09976076	14.96	0.97
2460192.76651900	3.67	1.11
2460193.77734790	3.34	1.35
2460193.82599660	−1.97	1.31
2460195.76304918	−5.14	0.94
2460195.80161774	−2.75	1.05
2460195.83124630	−2.24	0.97
2460196.76153753	−7.40	1.02
2460196.80613649	−3.91	1.02
2460196.85435330	−4.87	0.94
2460198.74800479	11.49	0.91
2460198.81742941	7.85	0.87
2460198.84542413	5.39	0.77
2460200.74046532	−7.21	1.07
2460200.78534718	−2.20	1.08
2460200.83814583	−1.26	1.07
2460201.77332723	6.47	0.73
2460201.79622377	9.70	0.81
2460201.85800751	7.00	0.81
2460204.77482518	−21.49	0.96
2460204.80641455	−20.91	0.88
2460204.91623978	−15.53	0.99
2460272.70896174	8.38	0.92
2460272.71643373	11.46	0.98
2460272.72410032	11.83	1.07
2460272.73387913	10.94	0.96
2460272.74149438	14.75	0.98
2460272.74894656	14.15	1.10
2460272.75645266	13.54	1.01
2460272.76405543	14.87	0.98
2460272.77146772	14.92	0.92
2460272.78168415	13.15	0.95
2460272.78911734	16.08	1.07
2460272.79657609	15.12	1.10
2460272.80441531	13.52	0.97
2460272.81143582	13.67	1.02
2460272.81907260	13.19	1.03
2460272.82888544	11.59	1.04
2460272.83632523	13.13	1.07
2460272.84397265	10.70	1.14
2460272.85134004	11.59	1.10
2460272.85912790	8.78	1.12
2460272.86647520	10.47	1.14

Moreover, we suspect at least some of the correlated noise is due to instrumental drift that is unrelated to the stellar rotation period. Using the squared-exponential kernel, we are agnostic to the source of the RV jitter. Our covariance matrix takes the following form:

$$C_{i,j} = h^2 \exp\left[-\frac{(t_i - t_j)^2}{2\tau^2}\right] + [\sigma_i^2 + \sigma_{\text{jit}}^2]\delta_{i,j}, \qquad (1)$$

where $C_{i,j}$ is the covariance matrix, h is the amplitude of the squared-exponential kernel, τ is the correlation timescale, t_i is the time of each observation, $\delta_{i,j}$ is the Kronecker delta function (i.e., the white-noise component), σ_i are the nominal uncertainties produced by the RV pipelines, and σ_{jit} is a jitter term, in case we have underestimated the white-noise component. With this covariance matrix, our likelihood function is

$$\log \mathcal{L} = -\frac{N}{2}\log 2\pi - \frac{1}{2}\log|C| - \frac{1}{2}r^{\text{T}}C^{-1}r, \qquad (2)$$

where $\mathcal{L}$ is the likelihood function, N is the total number of RV measurements, and r is the residual vector: $r \equiv RV(t_i) - M(t_i)$, measured as the RV minus the model RV. The RV models are circular Keplerian, described by the RV semi-amplitude K, the orbital period P_{orb}, and the time of conjunction T_c. We imposed Gaussian priors on P_{orb} and T_c using the results of the transit modeling in Section 3.3.

We allowed all of the hyperparameters of the GP to float freely in our modeling of the combined KPF and CARMENES

Table 5
CARMENES RVs of TOI-6255

Time (BJD)	RV ($\mathrm{m\,s^{-1}}$)	RV Unc. ($\mathrm{m\,s^{-1}}$)
2460120.46393455	−3.06	1.62
2460120.51080524	−0.05	1.52
2460120.58599291	2.33	1.33
2460120.64040814	0.25	1.31
2460121.47968095	2.55	3.92
2460122.46464087	11.23	4.30
2460122.52944385	−0.20	2.53
2460122.56474435	2.99	2.34
2460122.60303551	−0.93	1.97
2460123.46324037	6.29	3.24
2460123.52151940	−3.84	1.94
2460123.57083056	−3.55	1.81
2460123.61803215	−3.06	1.74
2460124.46376153	−4.43	2.35
2460124.52255125	−5.01	1.82
2460124.57117621	−5.00	2.85
2460124.61768596	−0.29	1.90
2460126.46060562	0.59	3.39
2460126.49574863	4.84	2.23
2460126.56197642	3.09	1.83
2460126.60298822	5.36	1.55
2460160.37799236	5.27	3.90
2460160.42652334	1.76	2.57
2460160.48450259	1.42	3.46
2460160.52696557	3.37	3.23
2460160.57725878	5.95	2.67
2460160.62478288	3.84	2.38
2460164.37810974	−1.80	2.52
2460164.42647410	0.01	1.81
2460164.48147214	−1.44	2.08
2460164.53039479	−2.59	2.06
2460164.57831531	−4.88	2.46
2460164.63229627	−2.66	2.30

RV data set. The only exception is that we placed an ad hoc lower boundary on the correlation timescale $\tau > 1$ day, so that the GP does not subsume the planetary signal of TOI-6255 b on 5.7 hr. We again sampled the posterior distribution using an MCMC analysis with emcee. The procedure is similar to that presented in Section 3.3. The results are summarized in Table 2. The RV variation of TOI-6255 b is robustly detected with $K = 2.98 \pm 0.28$ m s^{-1}.

For readers who are concerned that a GP model may produce a spurious detection of planetary signals, we highlight the KPF observations taken on 2023 November 24 (see the inset panel of Figure 2). The continuous set of 21 exposures obtained that night show the expected RV variation over the 5.7 hr period of TOI-6255 b. The correlated noise component modeled by the GP (the blue dotted line) is essentially constant on such a short timescale. We are unable to detect another RV planet in the presence of the correlated noise.

4.4. Floating Chunk Offset Method

Another commonly used strategy for dealing with correlated noise in RV data sets is the Floating Chunk Offset method (e.g., Hatzes et al. 2011). If the planet of interest has an orbital period of less than 1 day, one can rely exclusively on RV variations observed during a single night and discard any information about RV variations between nights. In essence,

any long-term stellar activity or instrumental effects are removed by allowing each night to have an independent additive RV offset.

This method naturally requires multiple observations taken within a single night. We trimmed our RV data sets by removing the isolated exposures. We were left with 106 data points taken on 29 different calendar nights, each given an offset γ_1 to γ_{29}. In this model, the only major change to the covariance function (Equation (1)) is that we have dropped the squared-exponential kernel and only retained the white-noise component. The likelihood is unchanged, other than the implicit inclusion of the nightly offsets in $RV(t_i)$.

We again used emcee to sample the posterior distribution, following a similar procedure as in the previous section. The Floating Chunk Offset method was able to robustly detect TOI-6255 b as well, yielding the RV semi-amplitude $K = 2.93 \pm 0.38$ m s^{-1}. This is fully consistent with the value determined in the GP model. Figure 3 compares the detection of TOI-6255 b using the GP and Floating Chunk Offset models. The GP model has far fewer parameters than the Floating Chunk Offset model and makes use of more data points. We adopted the GP model for all further analyses in this paper.

5. Discussion

5.1. Core Compositions

With precise mass and radius measurements in hand, we can now investigate the possible compositions of TOI-6255 b. To put TOI-6255 b into context, we queried the NASA Exoplanet Archive[68] for the latest sample of terrestrial planets ($<1.8 R_\oplus$) with well-measured masses and radii (both with $<20\%$ uncertainties). The sample is shown in Figure 4. We further identified a subsample of USP planets ($R_p < 1.8 R_\oplus$, $P_{\mathrm{orb}} < 1$ day; the blue symbols in Figure 4) to compare with TOI-6255 b. Previous studies (Sanchis-Ojeda et al. 2014; Lundkvist et al. 2016; Lopez 2017; Kreidberg et al. 2019b; Crossfield et al. 2022) have suggested that USP planets are so strongly irradiated by their host stars that any primordial H/He envelope should have been completely stripped away by intensive atmospheric erosion (Owen & Wu 2017; Ginzburg et al. 2018). As such, one can directly probe the planetary composition of these planets without worrying about a low-mean-molecular-weight atmosphere. Indeed, Dai et al. (2019) have shown that the measured masses and radii of USPs are consistent with expectations for atmosphere-free rocky planets with an Earth-like composition of roughly 30% Fe–70% silicate rocks.

To fully characterize the composition of TOI-6255 b, we explore two models. The first model is a two-layer interior model with an iron core and a silicate mantle (Zeng et al. 2016). The composition can be parameterized by a single number: the iron core mass fraction (CMF). We find that the CMF of TOI-6255 b is 0.45 ± 0.32 using this model. Figure 4 shows TOI-6255 b in comparison with other rocky exoplanets. We also employ the more sophisticated model SUPEREARTH (Valencia et al. 2007). SUPEREARTH further distinguishes between the true iron mass fraction (Fe–MF; Plotnykov & Valencia 2024) and the CMF. This is to account for the fact that the silicate mantle may contain iron, while the iron core may contain other elements. Following the method in Plotnykov & Valencia (2020), we included different degrees
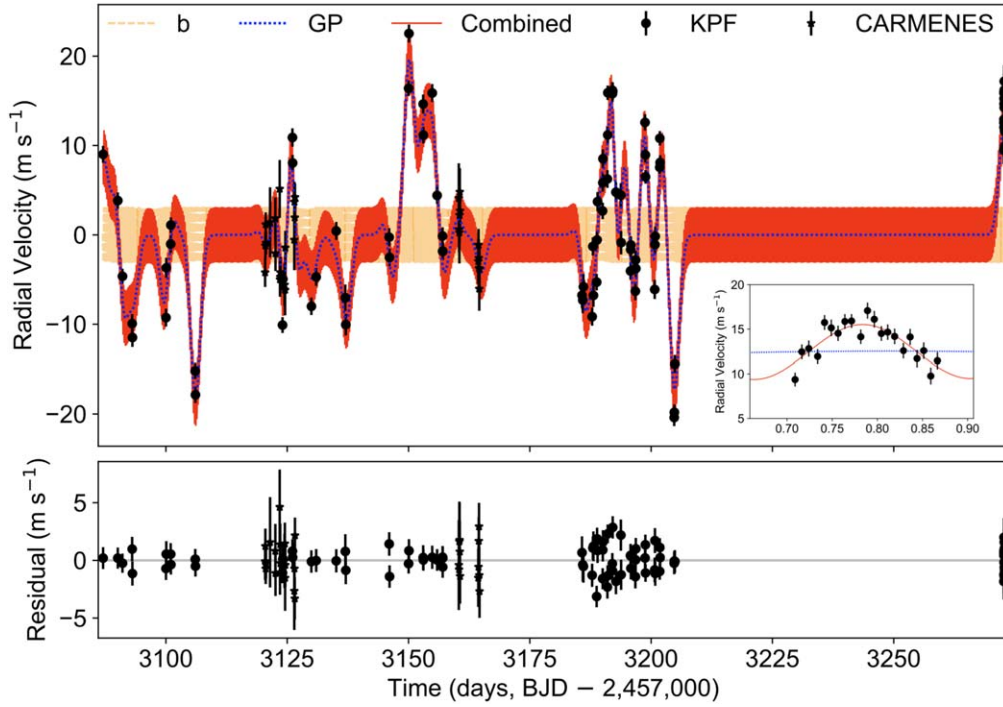
---

[68] https://exoplanetarchive.ipac.caltech.edu

Figure 2. RV variations of TOI-6255 b (orange dashed line) measured by KPF (circles) and CARMENES (stars). A GP model (blue dotted line) has been included to remove any stellar activity and instrumental variation on timescales longer than the orbital period of TOI-6255 b. On 2023 November 24, we took a set of 21 continuous exposures of TOI-6255 with KPF (inset). The resultant RVs clearly reveal the 5.7 hr orbit of TOI-6255 b.

of core differentiation (expressed as the amount of iron in the mantle, x_{Fe}) and different values for the Si alloy in the core (x_{Si}). We use priors on these values based on the terrestrial planets $x_{Fe} \sim U(0, 20)\%$ by mol and $x_{Si} \sim U(0, 20)\%$ by mol. Using an MCMC scheme, we found that TOI-6255 b has a $CMF = 0.41 \pm 0.20$ and $Fe\text{–}MF = 0.38 \pm 0.15$. These results are in agreement with the simpler model of Zeng et al. (2016). A magma ocean may be present on TOI-6255 (see the later discussion); Boley et al. (2023) have shown that the presence of a magma ocean imposes negligible change on the inferred composition of a rocky planet from mass and radius measurements. On the other hand, the significant tidal distortion of TOI-6255 may affect the inference on its composition, as will be explained in the next section.

5.2. Tidal Distortion

Given the extremely short orbital period of TOI-6255 b, it may be significantly tidally deformed. To demonstrate that TOI-6255 b is under extreme tidal stress, we first compared its orbital period to the Roche limit of an incompressible fluid:

$$P_{Roche} \approx 12.6 \, h \left(\frac{\rho_p}{1 \, g \, cm^{-3}} \right)^{-1/2}, \tag{3}$$

as in Rappaport et al. (2013). P_{Roche} is the orbital period of the Roche limit where tidal forces due to the star are stronger than the gravity of the planet, i.e., the planet starts to disintegrate if the material strength is negligible. The orbital period of TOI-6255 b is dangerously close to the Roche limit, with $P_{orb}/P_{Roche} = 1.13 \pm 0.10$. Figure 5 shows that although dozens of USP planets have been discovered, TOI-6255 b stands out as the planet that is closest to tidal disruption.

One can estimate the extent of tidal distortion of the planet using the Love number h_2 (Love 1944). For a homogeneous solid planet,

$$\delta R_p = h_2 \zeta, \tag{4}$$

$$h_2 = \frac{5/2}{1 + \tilde{\mu}}, \tag{5}$$

$$\tilde{\mu} = \frac{19\mu}{2\rho g R_p}, \tag{6}$$

$$\zeta = \frac{M_\star}{M_p} \left(\frac{R_p}{a} \right)^3 R_p, \tag{7}$$

where R_p and δR_p are the nominal radius and tidal distortion of the planet, M_p and $M_\star$ are the masses of the planet and the host star, μ is the tensile strength of the planet, ρ is the mean density of the planet, g is the surface gravity of the planet, and a is the semimajor axis. These quantities have been directly measured, with the exceptions of h_2 and μ. For a centrally concentrated planet, h_2 is further reduced from $\frac{5/2}{1 + \tilde{\mu}}$. Kellermann et al. (2018) showed that increasing the iron CMF of an Earth-sized planet from zero to Earth-like (30%) leads to roughly a factor 2 reduction in the tidal Love number. As for the tensile strength μ, Murray & Dermott (1999) recommend a mean tensile strength of 50 GPa for rocky bodies within the solar system; this would further reduce h_2 by a factor of $(1 + \tilde{\mu}) \approx 1.9$. However, for TOI-6255 b, the high equilibrium temperature ($\sim$1300 K) likely leads to at least partial melting and hence significant weakening of the tensile strength of the surface rocks (Takahashi 1986). Saiang & Miskovsky (2011) showed that from room temperature to 1000 K, the tensile strength of common rocks can easily drop by an order of magnitude.
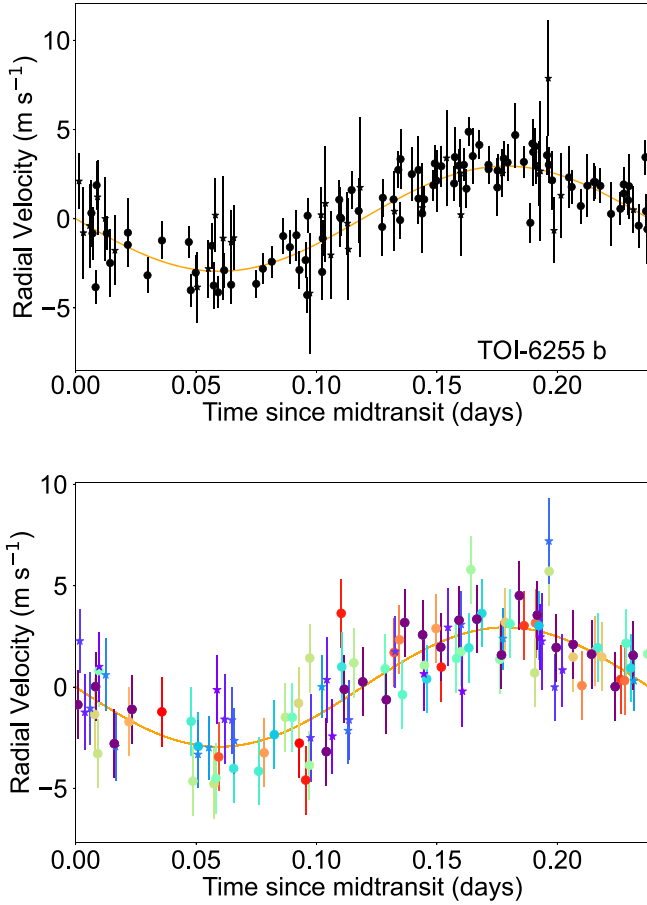
Figure 3. The RV variation of TOI-6255 b plotted as a function of the orbital phase. Top: the results of our GP model, where long-term stellar activities and instrumental effects have been removed before plotting. Bottom: an alternative model (Floating Chunk Offset; Section 4.4), where observations taken on a single calendar night were given an independent offset (plotted with a different color). These two models give consistent results on the RV semi-amplitude of TOI-6255 b ($K = 2.98 \pm 0.28$ m s^{-1} vs. $K = 2.93 \pm 0.38$ m s^{-1}).

Moreover, since the planet is likely in synchronous rotation and on a circular orbit (see Section 5.3 for tidal despin and circularization timescales), the tidal bulge on the planet is static in the corotating frame centered on the planet. Solid-body thermal creep (again, the equilibrium temperature is high enough) might have adjusted the planet to a hydrostatic equilibrium by slowly releasing any internal stress. Thus, $\tilde{\mu}$ can be negligible on TOI-6255 b. Empirically, estimates of Earth's Love number h_2 range between 0.6 and 0.9 (e.g., Lambeck 1980; Krásná et al. 2013). For TOI-6255 b, h_2 is likely higher than Earth, given the weakened material strength and larger planetary size. We adopt a fiducial $h_2 = 1$ for further analysis.

The 5.7 hr rotation period of TOI-6255 also leads to substantial rotational deformation:

$$q = \frac{\Omega^2 R_p^3}{GM_p}, \qquad (8)$$

where Ω is the rotational angular velocity of the planet, G is the gravitational constant, and q quantifies the surface gravity against the centrifugal force at the surface of the planet. q

amounts to about 4% on TOI-6255 b. For a synchronously rotating planet, it can be shown that the effective potential of the rotation is $-$one-third of the tidal potential (Murray & Dermott 1999). The tidal bulge is along the line connecting the host star and the planet (assuming a negligible tidal lag), while the rotational deformation bulges out the equator of the planet. The addition of these two effects results in an ellipsoidal shape (with semimajor axes $[R_1, R_2, R_3]$), as illustrated in Figure 6. The long axis R_1 points toward the host star. The intermediate axis R_2 points along the direction of orbital motion. The short axis R_3 is the polar axis parallel to the rotation axis of the planet. The three semi-axes of the ellipsoids are given by (see e.g., Correia 2014)

$$R_1 = R_{\rm vol}\left(1 + \frac{7}{6}\delta R_p\right), \qquad (9)$$

$$R_2 = R_{\rm vol}\left(1 - \frac{1}{3}\delta R_p\right), \qquad (10)$$

$$R_3 = R_{\rm vol}\left(1 - \frac{5}{6}\delta R_p\right), \qquad (11)$$

where $R_{\rm vol} \equiv (R_1 R_2 R_3)^{1/3}$ is the volumetric radius of the planet. A tidally distorted planet should also produce a distinct transit signal compared to a spherical model (Leconte et al. 2011). In particular, if the planet is in synchronous rotation, the long axis of the planet always points toward the star. Hence, the shadow of the planet projected on the star changes as a function of the orbital phase and orbital inclination:

$$A(\phi) = \pi\sqrt{R_1^2 R_2^2 \cos^2 i + R_3^2 \sin^2 i (R_1^2 \sin^2 \phi + R_2^2 \cos^2 \phi)}. \qquad (12)$$

For a transiting planet during transit, the orbital inclination i is close to 90° and the orbital phase ϕ is close to 0. R_1 is mostly hidden from the observer. Therefore, the transit radius of the planet is roughly given by $R_{\rm tran} \equiv (R_2 R_3)^{1/2}$. As such, the volumetric radius of the planet is larger than the transit radius of the planet: $R_{\rm vol} = R_{\rm tran}(1 + \frac{7}{12}\delta R_p)$.

We now revisit the composition of TOI-6255 b if we account for both tidal and rotational deformation. We can obtain the volumetric radius of the planet from its transit radius and the expected distortion. We then use the volumetric radius to infer the composition, primarily the iron CMF, of TOI-6255 b. Assuming $h_2 = 1$, this results in roughly a 3% increase in the transit radius. The inferred CMF of the planet drops from $45\% \pm 32\%$ to $31\% \pm 30\%$. Such a correction does not change the qualitative result presented in Section 5.1.

In principle, the ellipsoidal shape of the planet can be directly measured in the transit light curve and phase-curve variation. An ellipsoidal planet produces two major effects in the transit light curve: (1) it gives rise to an extension of the ingress/egress timescale, as the tidal bulge will occult the star before the nominal ingress of a spherical planet; and (2) the tidal bulge is hidden from the observer's view at mid-transit, but away from mid-transit, it slowly rotates into view and causes extra absorption compared to a spherical planet. We look for both effects in the TESS light curve by explicitly computing the transit light curve of an ellipsoidal planet (the lower panel of Figure 1). The light-curve correction due to an
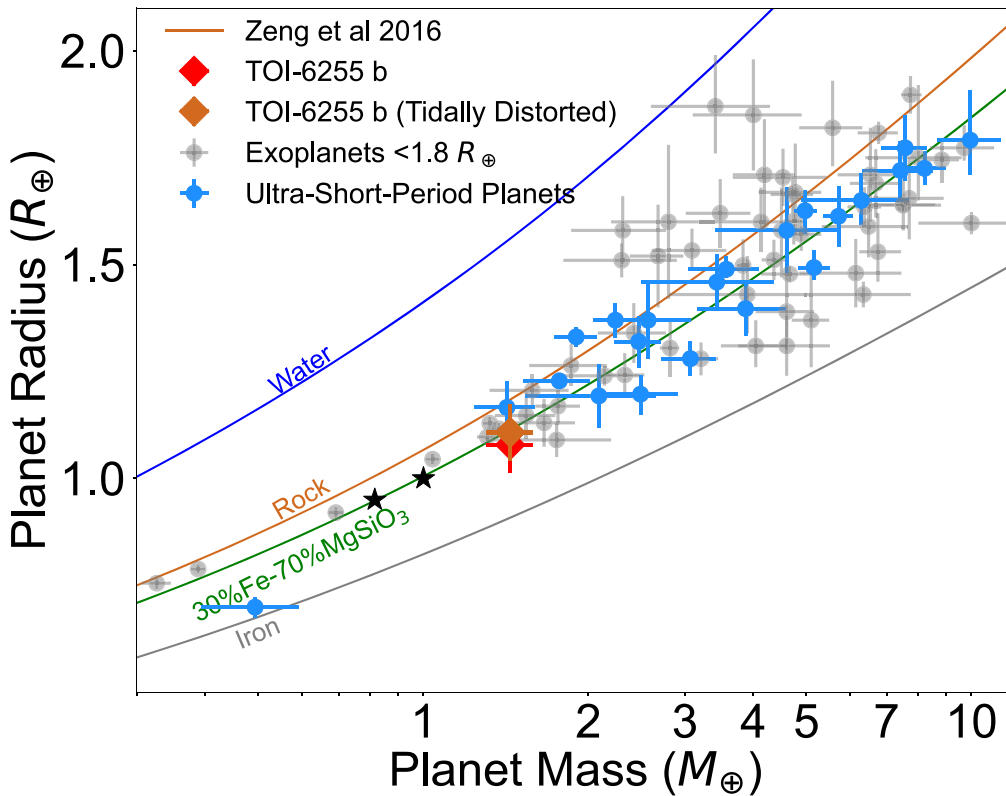
Figure 4. Precise mass and radius measurements of exoplanets $<1.8R_\oplus$ (from the NASA Exoplanet Archive) and theoretical mass–radius relationships (Zeng et al. 2019). The USP planets ($P_{orb} < 1$ day, $R_p < 1.8R_\oplus$; blue points) are so strongly irradiated that they should be bare rocky bodies devoid of H/He envelopes. The existing sample of USP planets is dominated by super-Earths ($>2M_\oplus$). As an ensemble, they cluster around an Earth-like 30% Fe–70% $MgSiO_3$ composition (Dai et al. 2019). TOI-6255 b is in the domain of Earth-sized planets. TOI-6255 b has a CMF of 45% ± 32% (red diamond). If accounting for the tidal distortion with a Love number $h_2 = 1$, the inferred CMF drops to a CMF of 31% ± 30%, because during transit the shorter two axes of the ellipsoidal planet are visible (brown diamond). See Section 5.2 for details.

ellipsoidal planet is <10 ppm. The binned uncertainty of the TESS light curve on a 2 minutes timescale (comparable to the ingress/egress timescale) is about 120 ppm. We could not robustly detect the signature of tidal distortion in the TESS light curve. Hellard et al. (2019) performed a detailed analysis of the detectability of tidal distortion in TESS data, finding that such a detection is challenging even for giant planets.

The calculation of the tidal and rotational deformation presented so far assumes small deformation and linear responses. In other words, the deformations are small compared to the size of the planet, and the different effects can be simply summed linearly. However, the tidal distortion on TOI-6255 b (~10%) is probably no longer linear, i.e., beyond the yield point of most solids (e.g., steel at ~0.1%; Ross 1999). In comparison, the lunar tide on Earth is of order 10^{-7}.

Previously, Price & Rogers (2020) expanded on the self-consistent field method of Hachisu (1986a, 1986b) to compute the tidal distortion of small, rocky planets in three dimensions, taking into account gravitational forces from the star and planet and the centrifugal force from the planet's rapid orbital motion. The model allows the planet to have an arbitrary number of layers. The Hachisu (1986a, 1986b) method is a relaxation procedure for solving the integro-differential equation governing the planet's equilibrium shape. In practice, the method rapidly converges to the equilibrium solution, within a specified tolerance, in just a few iterations.

We apply the model of Price & Rogers (2020) on TOI-6255 b. A potential limitation of the model of Price & Rogers (2020)

is that parameters of scientific interest—such as the orbital period, planet mass, and CMF—are outputs and cannot be specified upfront. For our purposes, we generated a library of models spanning a wide range of core–mantle boundary pressures, core pressures, aspect ratios, and planet–star distances. Within this model library, we drew and interpolated models that are broadly consistent with the measured stellar mass, planet mass, orbital period, and transit radius of TOI-6255 b. The results suggest that TOI-6255 b may indeed be more significantly distorted than what the Love theory predicts. The long axis may be 15% longer than the short axis. The model of Price & Rogers (2020) should be valid in the nonlinear regime of tidal distortion; however, it does not include material strength yet. In Love's linear theory of tidal distortion, material strength is included (see Equation (4)). It is not clear which model offers a better description of the tidal distortion of TOI-6255 b; nonetheless, the two models agree that TOI-6255 b is one of the most tidally distorted terrestrial planets discovered so far. We defer a detailed modeling of the tidal distortion to when it can be empirically constrained.

5.3. Tidal Decay and Dissipation

We have seen that TOI-6255 b may be tidally distorted due to its proximity to the Roche limit. Is it in any danger of being tidally disrupted in the near future? Using the constant-lag-angle model of equilibrium tides (Goldreich & Soter 1966; Winn et al. 2018), the tidal decay timescale due to tides raised
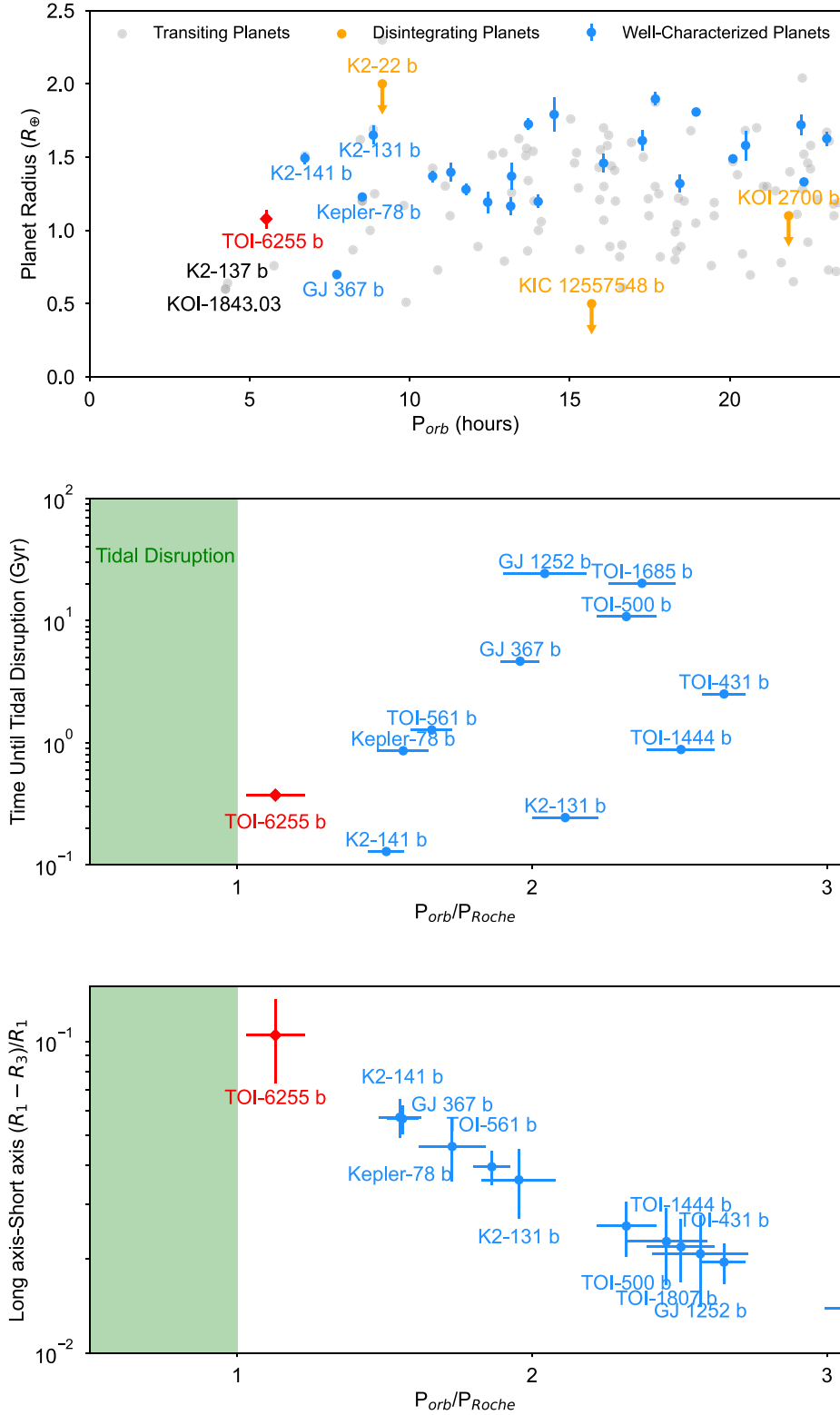
Figure 5. Top: with an orbital period of 5.7 hr and a semimajor axis ($a/R_\star = 3.1$), TOI-6255 b is close to the tidal disruption limit. K2-137 b (Smith et al. 2018) and KOI-1843.03 have shorter orbital periods. However, the masses of those planets are unknown. Middle: using the equation for the Roche limit $P_{\rm Roche} \approx 12.6$ hr $\times$ $(\rho_p/1 \, {\rm g \, cm}^{-3})^{-1/2}$ from Rappaport et al. (2013), one can compute how far a planet is away from tidal disruption $P_{\rm orb}/P_{\rm Roche}$. TOI-6255 b stands out as being on the verge of tidal disruption, with $P_{\rm orb}/P_{\rm Roche} = 1.13 \pm 0.10$. The y-axis is how fast the planet would reach the Roche limit due to equilibrium stellar tides (Equation (13); notice the strong dependence on orbital distance). TOI-6255 b may experience the fate of tidal disruption in the next 400 Myr if the tidal quality factor of the star $Q'_\star = 10^7$. The error bar is at least an order of magnitude due to the uncertainty on $Q'_\star$. Bottom: tidal distortion (the fractional difference between the long axis and the short axis of the ellipsoid) as predicted by tidal Love theory (Equation (4)) with a Love number $h_2 = 1$. TOI-6255 b is likely the most tidally distorted terrestrial planet discovered so far.
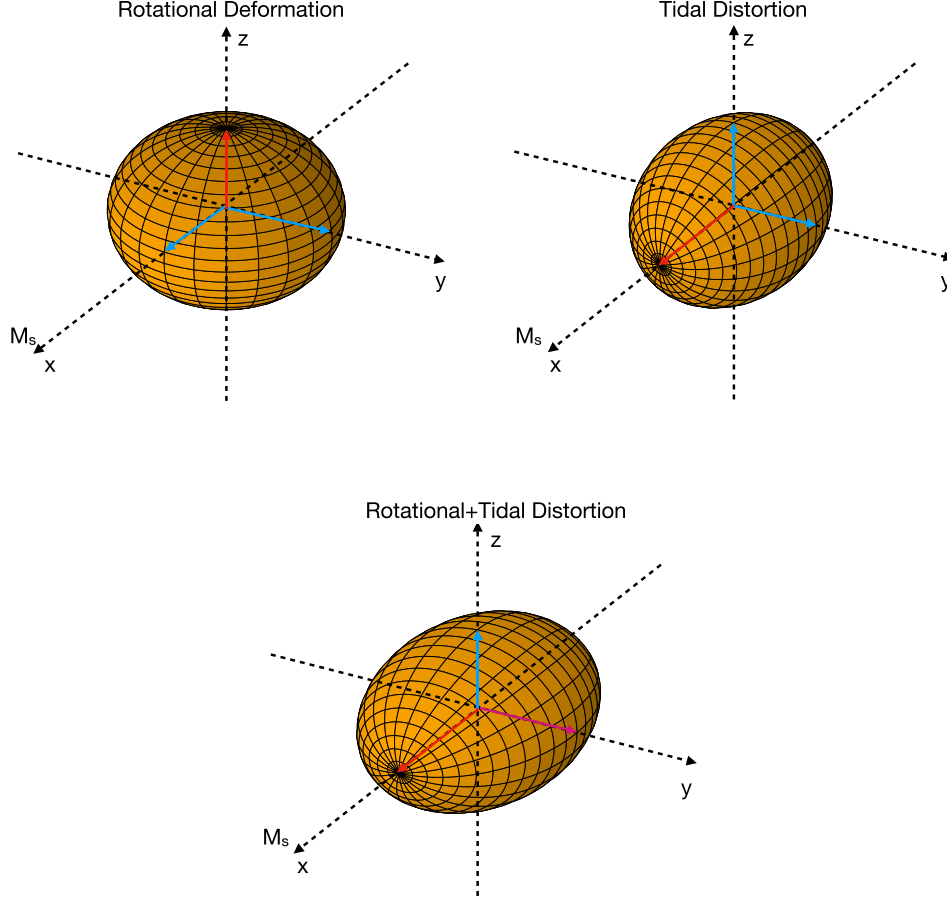
Figure 6. A schematic showing the rotational deformation (top left), tidal distortion (top right), and the combined effect for a synchronously rotating planet (bottom). The host star is located along the x-axis. The orbital motion is against the y-axis direction. The amount of distortion has been exaggerated for visualization. The red, magenta, and blue arrows indicate the long, intermediate, and short semi-axes of the ellipsoid ($[R_1, R_2, R_3]$). Rotational deformation produces an oblate planet with a bulge at the equator (see Equation (8)). Tidal distortion is along the axis joining the planet and the host star (see Equation (4)).

on the slowly rotating host star is given by

$$\frac{P}{\dot{P}} \approx 30 \, \text{Gyr} \left(\frac{Q'_\star}{10^6}\right)\left(\frac{M_\star/M_P}{M_\odot/M_\oplus}\right)\left(\frac{\rho_\star}{\rho_\odot}\right)^{5/3}\left(\frac{P_{\text{orb}}}{1 \, \text{day}}\right)^{13/3}, \quad (13)$$

where $Q'_\star$ is the tidal quality factor for the host star, M_P and $M_\star$ are the masses of the planet and the host star, and $\rho_\star$ is the mean stellar density. Using a nominal $Q'_\star = 10^7$ for the host star, TOI-6255 b has a tidal decay timescale of $\tau_P \equiv P/\dot{P} \approx 3.7$ Gyr. However, the orbital period only needs to change by $\sim 13\%$ to reach the Roche limit, which takes about $\tau_{\text{Roche}} \approx 400$ Myr if integrating Equation (13) (note the difference between τ_P and τ_{Roche}). The major source of uncertainty of this calculation comes from the tidal quality factor of the host star $Q'_\star$, which may vary by more than an order of magnitude and may be frequency-dependent, as suggested by recent theoretical and empirical results (e.g., Ogilvie 2014; Weinberg et al. 2017; Penev et al. 2018; Bailey et al. 2022). $Q'_\star = 10^7$ represents a relatively slow stellar dissipation rate (Penev et al. 2018). TOI-6255 is likely a mature M-star with an age of several gigayears, as evidenced by the

slow rotation. Tidal perturbation by a USP around a slowly spinning host star is outside the inertial range rendering the suppression of the dynamical tide (Ogilvie & Lin 2007).

A priori, it is unlikely that a planet would be discovered right before its destruction. As shown in Section 2, 400 Myr represents about 5%–10% of the system's age. More than a hundred USPs have been confirmed in the literature. In this light, it seems possible that the sample contains a planet whose tidal decay timescale is 5%–10% of the system's age. Figure 5 shows the time required for TOI-6255 b and other shortest-period planets to reach the tidal disruption limit τ_{Roche}. Among the USPs ($P_{\text{orb}} < 1$ day), the timescales can be shorter than the age of the Universe or the age of the host star. Once the planet is disrupted, the resultant debris is likely to fall onto the host star. Depending on how permeable the radiative–convective boundary is, the refractory elements may linger in the surface convective layer. The photospheric composition of a star would thus be enhanced in refractory elements found in rocky planets. By comparing the abundance of refractory elements on the photospheres of comoving, conatal binaries, it has been suggested that the star that is preferentially enriched in refractory elements experienced the engulfment of rocky

planets (Ramírez et al. 2015; Oh et al. 2018; Nagar et al. 2019; Galarza et al. 2021; Spina et al. 2021; Behmard et al. 2023; Liu et al. 2024). TOI-6255 b may be a progenitor of such a catastrophic planet engulfment event.

If TOI-6255 b still has a nonzero orbital eccentricity, tidal dissipation may take place in the planet. If so, the orbital decay rate can be sped up by including an additional term due to the tidal dissipation in the planet:

$$
\frac{P}{\dot{P}} \approx 2\mathrm{Gyr} \left(\frac{Q_p'}{10^3} \right) \left(\frac{M_p}{M_\oplus} \right) \left(\frac{M_\star}{M_\odot} \right)^{2/3}
$$

$$
\left(\frac{R_p}{R_\oplus} \right)^{-5} \left(\frac{P_{\mathrm{orb}}}{1\,\mathrm{day}} \right)^{13/3} \left(\frac{e}{0.01} \right)^{-2}. \tag{14}
$$

Using a nominal planetary tidal quality factor $Q_p' = 1000$, similar to Mars (Murray & Dermott 1999), and an e of 0.001 level (see that Io's eccentricity is about 0.004; Peale et al. 1979), the tidal decay timescale for TOI-6255 b is about $\tau_P \approx 200$ Myr. The tidal dissipation amounts to ~7% of the insolation the planet receives. Again, the major source of uncertainty is in Q_p', whose uncertainty can be more than an order of magnitude. Peale et al. (1979) pointed out that as the planet's core gets molten, the solid mantle gets increasingly thinner. The mantle experiences stronger deformation and thus stronger dissipation. On the other hand, if the planet's interior is completely molten (by tidal heating or by star–planet magnetic interaction; Section 5.4), the fluid-like interior is much less dissipative. Q_p' can be orders of magnitude higher, similar to the giant planets.

Equally important, can TOI-6255 b maintain a nonzero eccentricity? The tidal circularization time is given by:

$$
\tau_e \equiv \frac{e}{\dot{e}} \approx 0.7 \text{ Myr} \left(\frac{Q_p'}{10^3} \right) \left(\frac{M_p/M_\star}{M_\oplus/M_\odot} \right)
$$

$$
\left(\frac{R_\star/R_p}{R_\odot/R_\oplus} \right)^5 \left(\frac{\rho_\star}{\rho_\odot} \right)^{5/3} \left(\frac{P_{\mathrm{orb}}}{1\,\mathrm{day}} \right)^{13/3}. \tag{15}
$$

For TOI-6255 b, this is only $\tau_e \approx 400$ yr if Q_p' is 10^3. We briefly note that the tidal despin timescale for TOI-6255 b to become tidally locked is even shorter, by a factor $(R_p/a)^2$, and can be shorter than 1 yr for TOI-6255 b at its current orbital period. Such a short timescale justifies our earlier assumption that the planet is tidally locked with a constant dayside and nightside.

Given the short tidal circularization timescale, the planet should have a circular orbit, unless the other planets constantly pump up the eccentricity through resonant or secular interaction (e.g., Schlaufman et al. 2010; Petrovich et al. 2019; Pu & Lai 2019). Previous works have shown that USP planets like TOI-6255 b are almost always found in multiplanet systems (Winn et al. 2018; Dai et al. 2021). Hansen & Murray (2013) proposed a scenario for 55 Cnc e in which the planet maintains a nonzero eccentricity due to the perturbation of other planetary companions. We are currently unable to confirm any additional planets around TOI-6255 that could pump up the eccentricity of TOI-6255 b. Without an orbital eccentricity, most of the tidal dissipation happens within the host star, as described by Equation (13).

5.4. Star–Planet Magnetic Interaction

It has long been suspected that USP planets like TOI-6255 b may be within the stellar Alfvénic sphere and experience a strong star–planet magnetic interaction (e.g., Cuntz et al. 2000). The interaction is much analogous to our Io–Jupiter system (Bigg 1964). The transfer of ions from the planet back to the star, through a structure often referred to as the Alfvén wings, may lead to radio emission from the system (Zarka 1998). The associated ohmic dissipation may also give rise to orbital decay and the melting of the interior of the planet (in addition to the tidal effect; Laine & Lin 2012; Wei & Lin 2024). TOI-6255 b is a top candidate for detecting such star–planet magnetic interactions.

The decameter radio emission from Jupiter is likely due to the electron cyclotron maser (ECM) instability (Melrose & Dulk 1982; Zarka 1998). Star–planet magnetic interactions are capable of generating auroral radio emission from both the star and the planet. This nonthermal emission would have a characteristic gyrofrequency of $\nu_G = 2.8\,B$ MHz, where B is the local magnetic field (in Gauss). The emission would be coherent, broadband ($\Delta\nu \sim \nu_G/2$), and highly circularly polarized (probably reaching close to 100%, in some cases). Moreover, the stellar radio emission may be modulated by the orbital phase of the planet, just like Jupiter's decameter emission.

We note that any potential emission coming from the planet would most likely be undetectable, as the magnetic field strengths of rocky planets in the solar system do not exceed a few Gauss. The resulting ECM frequency is below Earth's ionosphere cutoff. On the other hand, the stellar magnetic field could reach a few hundred Gauss or even a few kilogauss (Saar & Linsky 1985). Spectropolarimetry has been used to infer a surface magnetic field strength for many nearby M dwarfs using Zeeman Doppler Imaging (e.g., Moutou et al. 2016, 2017). Magnetic fields of hundreds of Gauss would make the stellar ECM emission detectable with current radio observatories, such as LOFAR (van Haarlem et al. 2013) and FAST (Nan et al. 2011). We encourage follow-up observation of TOI-6255 using these radio telescopes.

5.5. Is TOI-6255 b Already Disintegrating?

Given TOI-6255 b's proximity to the Roche limit (see Section 5.2), one may wonder whether TOI-6255 b is already losing mass, making it similar to the "disintegrating planets" KOI-2700 b (Rappaport et al. 2014), KIC 12557548 b (Rappaport et al. 2012), and K2-22b (Sanchis-Ojeda et al. 2015). All three of those disintegrating planets have longer orbital periods than TOI-6255 b (Figure 5). The transits of all three disintegrating planets are notably asymmetric (egress can be several times longer than ingress) about the mid-transit times, and there can be an order of unity change in the transit depths over time. The prevailing explanation is that we are observing a tail of dusty materials episodically emanating from these planets (van Lieshout & Rappaport 2018). See also the upcoming JWST observations of K2-22 b by N. Tusay et al. (2024, in preparation; Program 3315). In addition, due to their material strength, debris up to kilometer size and less conspicuous from an ongoing disrupting planet may be preserved, despite the intense tidal tearing in the proximity of the host star's surface (Zhang et al. 2021).

We show that TOI-6255 b is likely not undergoing catastrophic disintegration. We did not detect any asymmetry in the TESS transit signal. We fitted a simple trapezoidal model to the phase-folded light curve, similar to Sanchis-Ojeda et al.

(2015), and found no statistically significant difference between the ingress and egress of the light curve. Moreover, the transit depth of TOI-6255 b also appears to be constant. The standard deviations of the in-transit and out-of-transit flux residuals of each TESS 2 minute exposure are almost identical (1415 ppm versus 1429 ppm). Moreover, the transit depths in TESS Sectors 16 and 56 (separated by 3 yr) are consistent within 1σ of each other. Perez-Becker & Chiang (2013) showed that catastrophic evaporation only takes place on small (0.1 $M_\oplus$), strongly irradiated (2000 K) planets (i.e., a high thermal sound speed and low escape velocity from the planet). TOI-6255 b (1.44 $M_\oplus$) is likely too massive to undergo this mode of mass loss, although with its $P_{orb}/P_{Roche} \simeq 1.13$, Roche-lobe overflow of the planet's atmosphere may significantly ease this stringent requirement (Li et al. 2010).

5.6. Why Do the Shortest-period Planets Orbit Late-type Stars?

An intriguing observation is that TOI-6255 b and other top contenders for the shortest-period planet—KOI-1843.03 (4.2 hr, M1 host; Ofir & Dreizler 2013; Rappaport et al. 2013), K2-137 b (4.3 hr, M3 host; Smith et al. 2018), K2-141 b (6.7 hr, K7 host; Barragán et al. 2018), and GJ-367 b (7.7 hr, M1 host; Lam et al. 2021)—are all around late-type stars. The disintegrating planets are also all around K- or M-type host stars. Sanchis-Ojeda et al. (2014) showed that the occurrence rate for USPs is about $0.15\% \pm 0.05\%$ for F stars, $0.51\% \pm 0.07\%$ for G stars, but increases to $1.1\% \pm 0.4\%$ for M dwarfs. Why are the shortest-period planets found around late-type stars? What would be the implication for planet formation at the inner edge of the protoplanetary disks?

Lee & Chiang (2017) noted that the inner edge of the protoplanetary disk plays a pivotal role in setting the lower boundary for the orbital periods of planets. Magnetospheric disk truncation is expected to happen at the corotation radius set by the rotation period of the host star. Rotation measurements of young clusters (see, e.g., Figure 2 of Bouvier 2013) have indeed indicated that late-type stars tend to maintain fast rotation throughout the timescale of planet formation (with periods often <3 days on 10 Myr timescales). On the other hand, Sun-like stars tend to spin down faster even before the planetary disk dissipates. It could be the case that the smaller disk inner edge around late-type stars enables the formation of more short-period planets like TOI-6255 b, before tides further shrink their orbits over gigayear timescales.

5.7. JWST Phase-curve Observations

USP planets like TOI-6255 b are particularly amenable to phase-curve and secondary eclipse observations with JWST (Gardner et al. 2006). The flux ratio between USPs and their host stars is at a favorable level of a few hundred parts per million in the infrared. Furthermore, the USPs are expected to be fully tidally locked with their host star (Winn et al. 2018), resulting in a constant dayside and a constant nightside. Phase-curve observations map out the temperature distribution as a function of longitudes on the planet (Koll & Abbot 2015), in turn providing insights into the presence or absence of an outgassed, high-molecular-weight atmosphere (Demory et al. 2016). In the absence of an atmosphere, the same measurements may directly probe the surface mineralogy on these planets (Hu et al. 2012; Kreidberg et al. 2019b; Zhang et al. 2024). The stellar insolation TOI-6255 b receives is about $590 \pm 90 F_\oplus$; the equilibrium temperature is 1340 ± 60 K, assuming a low albedo of 0.1 appropriate for a dark
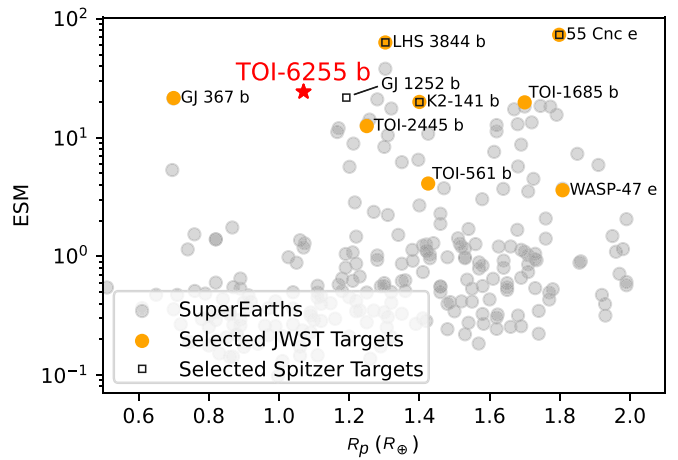
Figure 7. The ESM (Kempton et al. 2018) vs. planet radius, for planets smaller than 2 $R_\oplus$ (super-Earths). TOI-6255 b has an ESM of 24 and hence is more favorable than many planets for which JWST observations have already been scheduled (orange). It is also the most Earth-like in size among the currently confirmed exoplanet sample.

basaltic surface (Essack et al. 2020). The dayside may have a different extent of lava pool, depending on the detail of heat transport and if there is substantial tidal heating (Kite et al. 2016).

Nine USP planets (GJ 367 b, K2-141 b, 55 Cnc e, LHS 3844 b, TOI-561 b, WASP-47 e, TOI-1685 b, TOI-4481 b, and TOI-2445 b) have been selected as JWST targets. The majority of these are super-Earths (>1.2 $R_\oplus$; Figure 7). This preference for super-Earths is mainly driven by S/N considerations, as the Emission Spectroscopy Metric (ESM; Kempton et al. 2018) is proportional to $(R_p/R_\star)^2$. TOI-6255, on the other hand, is an Earth-sized planet (1.079 ± 0.065 $R_\oplus$) on a 5.7 hr orbit around a nearby M dwarf ($K = 8.1$). It boasts an ESM of 24, making it a top ESM rocky planet for phase-curve observations with MIRI/LRS, trailing only LHS 3844 b (Vanderspek et al. 2019) and 55 Cnc e (Winn et al. 2011; Crida et al. 2018).

Finally, we examine how the tidal distortion of a planet can modify the phase-curve variations. The obvious effect is the ellipsoidal light variation (ELV). Since TOI-6255 b is likely in synchronous rotation, the long axis of the ellipsoidal planet always points toward the star. Hence, at different orbital phases, we should see a different projection of the planet as described in Equation (12), which roughly scales as ($\sqrt{\sin^2(\phi)}$; ϕ is the orbital phase). The projection effect has two peaks at both quadratures of the orbit. To first order, phase-curve variations of the planet will be modulated by this area projection effect. This effect is analogous to the ELV of the binary stars (e.g., Morris 1985). For TOI-6255, we calculate that the stellar ELV is <1 ppm, whereas the planetary ELV is tens of parts per million in amplitude, depending on the tidal Love number and the strength of thermal emission. The planetary ELV is directly proportional to the change of the projected area of the tidally distorted planet (i.e., a 10% fractional area change, depending on the tidal Love number h_2). In principle, the planetary ELV can be distinguished from the thermal phase curve. The thermal emission of a bare rocky planet only peaks at the secondary eclipse, whereas the ELV peaks at quadratures ($-\cos(\phi)$ versus $\sqrt{\sin^2(\phi)}$). The tidal distortion of TOI-6255 may further modify the phase-curve variation through geological effects. The long axis of the planet (i.e., at the substellar and antistellar points) is where the silicate mantle is the thickest, and the thicker mantle there may

promote convection and volcanic activity. This effect would result in an even hotter substellar point. However, a proper simulation of this effect and its observability with JWST requires a dedicated model; we defer that to future work.

6. Summary

In this work, we present the discovery and confirmation of TOI-6255 b using transit observations and Doppler monitoring of the host star. We summarize the key findings as follows:

1. TOI-6255 b has an orbital period of 5.7 hr and a transit radius of $1.079 \pm 0.065 \, R_\oplus$.

2. By applying both GP regression and the Floating Chunk Offset method on the KPF and CARMENES RV measurements, we constrained the mass of TOI-6255 b to be $1.44 \pm 0.14 \, M_\oplus$.

3. TOI-6255 b has an iron CMF of $45\% \pm 32\%$ (Zeng et al. 2016; or $41\% \pm 20\%$, if using the model by Plotnykov & Valencia 2020), which is broadly consistent with an Earth-like composition.

4. TOI-6255 b experiences extreme tidal forces. It is marginally outside the Roche limit, with $P_{\rm orb}/P_{\rm Roche} = 1.13 \pm 0.10$ (Rappaport et al. 2013). The planet would tidally decay to the Roche limit within the next 400 Myr if the host star's reduced tidal quality factor is $Q'_\star = 10^7$. The resultant tidal disruption may produce the long suspected planet engulfment signature.

5. TOI-6255 b may experience star–planet magnetic interaction analogous to our Io–Jupiter interaction. The resultant radio emission may be orbital-phase-modulated and circularly polarized.

6. TOI-6255 b is likely ellipsoidal in shape. Assuming a tidal Love number $h_2 = 1$, the planet's long axis is about 10% longer than its short axis. Accounting for this effect, the CMF of the planet is reduced to $31\% \pm 30\%$. The ellipsoidal shape produces a subtle distortion of the transit light curve (<10 ppm) that could not be detected with the existing TESS data.

7. With an ESM of 24, TOI-6255 b is a top-ranking target for JWST phase-curve variation observations, which may determine the presence/lack of a heavy-mean-molecular-weight atmosphere. If the planet is a bare rocky core, emission spectra may tell us the dominant surface mineralogy. The ellipsoidal shape of TOI-6255 further modifies the phase-curve variation; the planetary ELV should enhance planetary emission near quadratures of the orbit.

Facilities: Keck:I (KPF), 3.5m Calar Alto, TESS, LCOGT, MuSCAT2, MuSCAT3, WASP, Palomar.

Software: ASTROIMAGE (Collins et al. 2017), ISOCLASSIFY (Huber et al. 2017), ISOCHRONES (Morton 2015), MIST (Choi et al. 2016), SPECMATCH-SYN (Petigura 2015), BATMAN (Kreidberg 2015), EMCEE (Foreman-Mackey et al. 2013).

Appendix A
Supplementary Figures

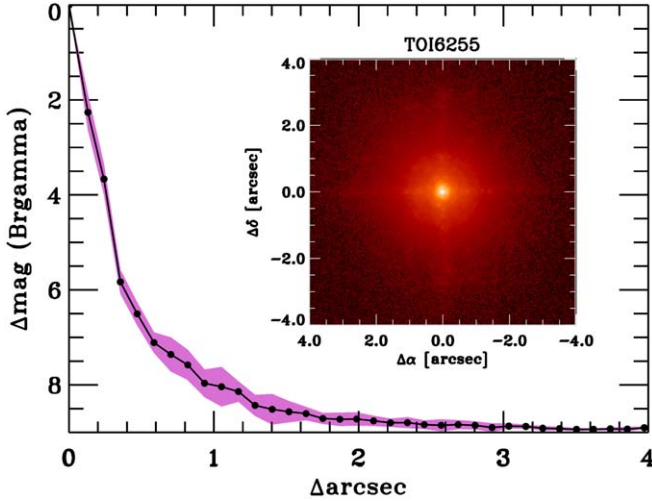Figure A1 shows the high-resolution imaging of TOI-6255 with Palomar/PHARO.

Figure A1. The contrast curve as function of radial distance from TOI-6255 using Palomar/PHARO observations (Hayward et al. 2001). The inset shows the high-contrast image of TOI-6255. We could rule out companions <6.5 mag within at 0″.5.

Appendix B
Phase Curve and Secondary Eclipse

Given the extremely short orbital period of TOI-6255 b, we searched for any phase-curve variation or secondary eclipse in the TESS light curve. We removed data taken during the transits of TOI-6255 b. We then detrended any long-term stellar variability and instrumental effects, following the method of Sanchis-Ojeda et al. (2013). Briefly, for each data point in the original light curve, we isolated a window of $1\times$, $2\times$, or $3 \times P_{orb}$ the orbital period around that data point. We removed any 5σ outliers and then fitted a linear function of time to the remaining data points within that window. The original data point is then divided by the local best-fit linear function of time. We experimented with both the PDC-SAP and SAP TESS light curves as well as with using different window widths ($1\times$, $2\times$, or $3 \times P_{orb}$). The resultant phase-curve variations did not show any substantial differences between these choices. We report the results based on the SAP light curve and with a window width of $2P_{orb}$.
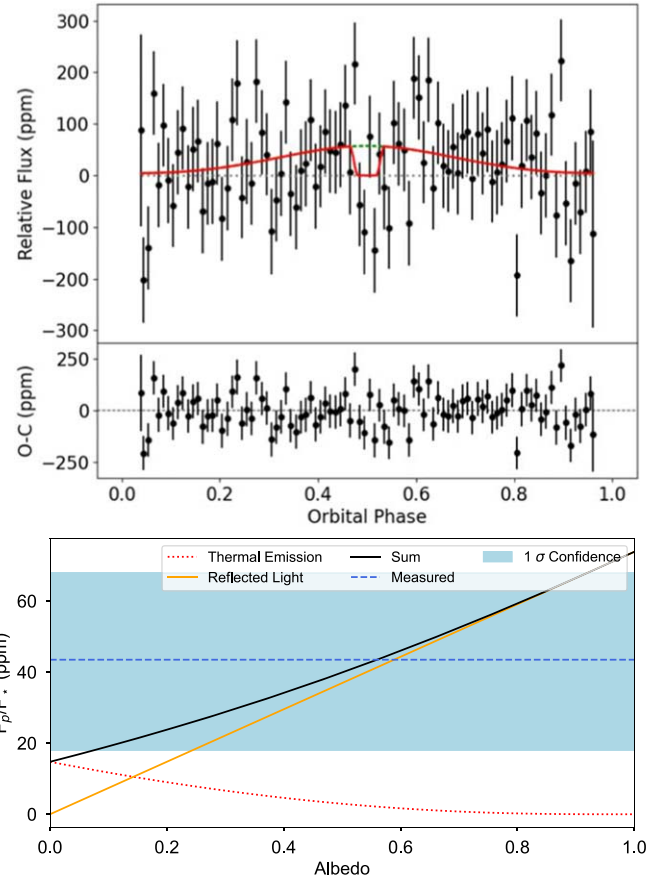

Figure B1. Top: the phase-curve variation of TOI-6255 b observed by TESS. The red curve shows the best-fit phase curve and secondary eclipse model. The phase curve is only detected at a 2σ level with two sectors of TESS observations in the optical. Bottom: the amount of thermal emission (red dotted line) and reflected light (orange solid line) in the TESS band as a function of the Bond albedo. The blue dashed line is the measured amount of planetary flux over the stellar flux ($F_p/F_\star$) and the associated 1σ confidence interval (blue area). The phase-curve variation in TESS is likely a combination of thermal emission and reflected light.

Our occultation (secondary eclipse) model uses the best-fit system parameters (period and orbital inclination, etc.) from the much more precise transit (primary eclipse) model (Section 3.3). The only difference is that the limb-darkening coefficients have been set to 0, and the secondary eclipse depth (δ_{sec}) is allowed to vary freely to account for a combination of reflected stellar light and thermal emission from the planet in the TESS band (600–1000 nm). The out-of-eclipse phase-curve variation is modeled as a Lambertian disk (see, e.g., Demory et al. 2016). This model is characterized by the amplitude of the illumination effect A and any phase offset of the peak of the phase curve θ. We initially let δ_{sec} and A vary independently, in essence allowing for a nonzero flux from the nightside of the planet. However, TOI-6255 has only been observed by TESS for two sectors and the S/N of the existing data does not support a statistically significant detection of the nightside flux or a phase offset (see Figure B1). We therefore report the results of the simplest phase-curve model where $\delta_{sec} \equiv A$ (no nightside contribution) and $\theta = 0$ (no phase offset). We sample the posterior distribution using another MCMC analysis with emcee (Foreman-Mackey et al. 2013). The procedure is similar to that described in the previous section. We find that $\delta_{sec} \equiv A_{ill} = 43 \pm 25$ ppm. This is less than the 2σ detection of the phase curve/secondary eclipse.

In Figure B1, we plot the ratio of planetary to stellar flux $F_p/F_\star$ in the TESS band as a function of the planet's Bond albedo. We assume that the albedo in the TESS band is the same as the Bond albedo. The higher the Bond albedo, the more the reflective the planet is, and the lower the equilibrium temperature will be. The planet reflects more stellar light but gives out weaker thermal emission. The blue shaded area is the 1σ confidence interval from TESS. The confidence interval is so wide that we cannot place a meaningful constraint on the planet's albedo. TOI-6255 b is a top-ranking target for future JWST phase-curve characterization in the near- and mid-infrared; any phase-curve variation of TOI-6255 will be much more observable in the infrared (see Section 5.7).

Appendix C
Transit Modeling with Other Light Curves

TOI-6255 b was observed by a suite of ground-based facilities, including the Las Cumbres Observatory Global Telescope (LCOGT; Brown et al. 2013) network nodes at the Teide Observatory (1 m telescope), the McDonald Observatory (1 m telescope), MuSCAT2 (1.5 m; Narita et al. 2019), and LCOGT MuSCAT3 (2 m; Narita et al. 2020).

Due to the small size of the transit signal (~ 0.7 mmag), only MuSCAT3 (the largest aperture) detected the transit signal robustly. We highlight the results from MuSCAT3 here. All other ground-based photometric observations can be downloaded from the ExoFOP website. MuSCAT3 is mounted on the 2 m Faulkes Telescope North at Haleakala Observatory on Maui, Hawai'i. MuSCAT3 has four simultaneous channels: g' (400–550 nm), r' (550–700 nm), i' (700–820 nm), and z_s (820–920 nm). We combined the four channels together in our photometric analysis using their weighted mean and a single set of limb-darkening coefficients.

TOI-6255 was observed by MuSCAT3 on UT 2023 August 14, August 18, September 8, September 28, and November 24. The images were calibrated using standard procedures by the BANZAI pipeline.[69] Differential photometric data were extracted using AstroImageJ (Collins et al. 2017), with circular photometric apertures having a radius 6″ or smaller that excluded flux from the nearest known neighbor (Gaia DR3 1956328333129802112) that is 9″ west of TOI-6255. We followed the same procedure as for our analysis of the TESS light curves. The phase-folded and binned MuSCAT3 light curve and the best-fit transit model are shown in Figure C1. The posterior distribution of the transit parameters is consistent with that from TESS, albeit with higher uncertainty. Notably, the MuSCAT3 observations also suggest a high impact parameter ($b = 0.77 \pm 0.09$) for TOI-6255 b (see $b = 0.84 \pm 0.05$ from TESS). MuSCAT3 suggests $R_p/R_\star = 0.0286 \pm 0.0031$, which agrees with the $R_p/R_\star = 0.0267 \pm 0.0014$ from TESS well within 1σ.

We also modeled the TESS Gaia Light Curve (TGLC; Han & Brandt 2023), which used point-spread function modeling to remove contamination from nearby stars in the TESS 200 s full-frame image light curves. The TGLC light curve is only available for Sector 56 for TOI-6255. We find that SPOC/PDC-SAP and TGLC produce consistent results on the radius of TOI-6255 b. The TGLC (Han & Brandt 2023) light curves also give a consistent $R_p/R_\star = 0.0273 \pm 0.0014$.

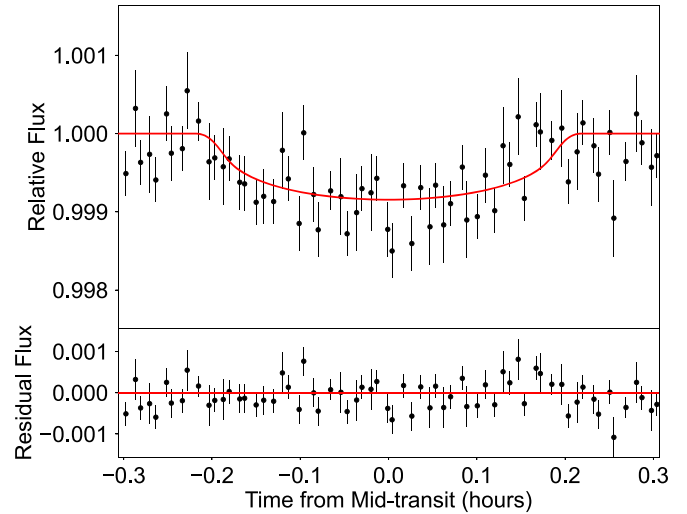[69] https://github.com/LCOGT/banzai

Figure C1. Phase-folded and binned MuSCAT3 (Narita et al. 2020) observation of TOI-6255 b. The transit parameters inferred from MuSCAT3 observations are consistent with those from TESS.

ORCID iDs

Fei Dai ● https://orcid.org/0000-0002-8958-0683
Andrew W. Howard ● https://orcid.org/0000-0001-8638-0320
Samuel Halverson ● https://orcid.org/0000-0003-1312-9391
Jaume Orell-Miquel ● https://orcid.org/0000-0003-2066-8959
Enric Pallé ● https://orcid.org/0000-0003-0987-1593
Howard Isaacson ● https://orcid.org/0000-0002-0531-1073
Benjamin Fulton ● https://orcid.org/0000-0003-3504-5316
Ellen M. Price ● https://orcid.org/0000-0002-3286-3543
Mykhaylo Plotnykov ● https://orcid.org/0000-0002-9479-2744
Leslie A. Rogers ● https://orcid.org/0000-0003-0638-3455
Diana Valencia ● https://orcid.org/0000-0003-3993-4030
Kimberly Paragas ● https://orcid.org/0000-0003-0062-1168
Michael Greklek-McKeon ● https://orcid.org/0000-0002-0371-1647
Jonathan Gomez Barrientos ● https://orcid.org/0000-0002-0672-9658
Heather A. Knutson ● https://orcid.org/0000-0002-5375-4725
Erik A. Petigura ● https://orcid.org/0000-0003-0967-2893
Lauren M. Weiss ● https://orcid.org/0000-0002-3725-3058
Rena Lee ● https://orcid.org/0000-0001-7058-4134
Casey L. Brinkman ● https://orcid.org/0000-0002-4480-310X
Daniel Huber ● https://orcid.org/0000-0001-8832-4488
Gumundur Stefánsson ● https://orcid.org/0000-0001-7409-5688
Kento Masuda ● https://orcid.org/0000-0003-1298-9699
Steven Giacalone ● https://orcid.org/0000-0002-8965-3969
Cicero X. Lu ● https://orcid.org/0000-0001-9352-0248
Edwin S. Kite ● https://orcid.org/0000-0002-1426-1186
Renyu Hu ● https://orcid.org/0000-0003-2215-8485
Eric Gaidos ● https://orcid.org/0000-0002-5258-6846
Michael Zhang ● https://orcid.org/0000-0002-0659-1783
Ryan A. Rubenzahl ● https://orcid.org/0000-0003-3856-3143
Joshua N. Winn ● https://orcid.org/0000-0002-4265-047X
Te Han ● https://orcid.org/0000-0002-7127-7643
Corey Beard ● https://orcid.org/0000-0001-7708-2364
Rae Holcomb ● https://orcid.org/0000-0002-5034-9476
Aaron Householder ● https://orcid.org/0000-0002-5812-3236
Gregory J. Gilbert ● https://orcid.org/0000-0003-0742-1660
Jack Lubin ● https://orcid.org/0000-0001-8342-7736
J. M. Joel Ong ● https://orcid.org/0000-0001-7664-648X
Alex S. Polanski ● https://orcid.org/0000-0001-7047-8681

Nicholas Saunders https://orcid.org/0000-0003-2657-3889
Judah Van Zandt https://orcid.org/0000-0002-4290-6826
Samuel W. Yee https://orcid.org/0000-0001-7961-3907
Jingwen Zhang https://orcid.org/0000-0002-2696-2406
Bradford Holden https://orcid.org/0000-0002-6153-3076
Max Brodheim https://orcid.org/0009-0008-9808-0411
Ian J. M. Crossfield https://orcid.org/0000-0002-1835-1891
William Deich https://orcid.org/0009-0000-3624-1330
Steven R. Gibson https://orcid.org/0009-0004-4454-6053
Grant M. Hill https://orcid.org/0000-0002-7648-9119
Sharon R Jelinsky https://orcid.org/0009-0006-2900-0401
Marc Kassis https://orcid.org/0000-0001-8414-8771
Russ R. Laher https://orcid.org/0000-0003-2451-5482
Kyle Lanclos https://orcid.org/0009-0004-0592-1850
Scott Lilley https://orcid.org/0000-0001-7323-7277
Joel N. Payne https://orcid.org/0009-0008-4293-0341
Paul Robertson https://orcid.org/0000-0003-0149-9678
Arpita Roy https://orcid.org/0000-0001-8127-5775
Christian Schwab https://orcid.org/0000-0002-4046-987X
Abby P. Shaum https://orcid.org/0000-0003-3133-6837
Martin M. Sirk https://orcid.org/0009-0007-8555-8060
Adam Vandenberg https://orcid.org/0009-0003-6534-0428
Josh Walawender https://orcid.org/0000-0002-6092-8295
Sharon X. Wang https://orcid.org/0000-0002-6937-9034
Shin-Ywan (Cindy) Wang https://orcid.org/0009-0002-4850-5377
Jason T. Wright https://orcid.org/0000-0001-6160-5888
Sherry Yeh https://orcid.org/0000-0002-4037-3114
José A. Caballero https://orcid.org/0000-0002-7349-1387
Juan C. Morales https://orcid.org/0000-0003-0061-518X
Felipe Murgas https://orcid.org/0000-0001-9087-1245
Evangelos Nagel https://orcid.org/0000-0002-4019-3631
Ansgar Reiners https://orcid.org/0000-0003-1242-5922
Andreas Schweitzer https://orcid.org/0000-0002-1624-0389
Hugo M. Tabernero https://orcid.org/0000-0002-8087-4298
Mathias Zechmeister https://orcid.org/0000-0002-6532-4378
Alton Spencer https://orcid.org/0000-0001-9263-6775
David R. Ciardi https://orcid.org/0000-0002-5741-3047
Catherine A. Clark https://orcid.org/0000-0002-2361-5812
Michael B. Lund https://orcid.org/0000-0003-2527-1598
Douglas A. Caldwell https://orcid.org/0000-0003-1963-9616
Karen A. Collins https://orcid.org/0000-0001-6588-9574
Richard P. Schwarz https://orcid.org/0000-0001-8227-1020
Khalid Barkaoui https://orcid.org/0000-0003-1464-9276
Cristilyn Watkins https://orcid.org/0000-0001-8621-6731
Avi Shporer https://orcid.org/0000-0002-1836-3120
Norio Narita https://orcid.org/0000-0001-8511-2981
Akihiko Fukui https://orcid.org/0000-0002-4909-5763
David W. Latham https://orcid.org/0000-0001-9911-7388
Jon M. Jenkins https://orcid.org/0000-0002-4715-9460
George R. Ricker https://orcid.org/0000-0003-2058-6662
Sara Seager https://orcid.org/0000-0002-6892-6948
Roland Vanderspek https://orcid.org/0000-0001-6763-6562

References

Allard, F. 2014, in IAU Symp. 299, Exploring the Formation and Evolution of Planetary Systems, ed. M. Booth, B. C. Matthews, & J. R. Graham (Cambridge: Cambridge Univ. Press), 271
Bailey, N., Gilbert, G., & Fabrycky, D. 2022, AJ, 163, 13
Barragán, O., Gandolfi, D., Dai, F., et al. 2018, A&A, 612, A95
Behmard, A., Dai, F., Brewer, J. M., Berger, T. A., & Howard, A. W. 2023, MNRAS, 521, 2969
Bensby, T., Feltzing, S., & Oey, M. S. 2014, A&A, 562, A71
Bigg, E. K. 1964, Natur, 203, 1008
Bland-Hawthorn, J., & Gerhard, O. 2016, ARA&A, 54, 529
Boley, K. M., Panero, W. R., Unterborn, C. T., et al. 2023, ApJ, 954, 202
Bouma, L. G., Kerr, R., Curtis, J. L., et al. 2022, AJ, 164, 215
Bouvier, J. 2013, in EAS Publications Ser. 62, Role and Mechanisms of Angular Momentum Transport During the Formation and Early Evolution of Stars, ed. P. Hennebelle & C. Charbonnel (Les Ulis: EDP Sciences), 143
Brown, T. M., Baliber, N., Bianco, F. B., et al. 2013, PASP, 125, 1031
Caballero, J. A., Guàrdia, J., López del Fresno, M., et al. 2016, Proc. SPIE, 9910, 99100E
Chiti, F., van Saders, J. L., Heintz, T. M., et al. 2024, arXiv:2403.12129
Choi, J., Dotter, A., Conroy, C., et al. 2016, ApJ, 823, 102
Cifuentes, C., Caballero, J. A., Cortés-Contreras, M., et al. 2020a, A&A, 642, A115
Cifuentes, C., Caballero, J. A., Cortés-Contreras, M., et al. 2020b, A&A, 642, A115
Collins, K. A., Kielkopf, J. F., Stassun, K. G., & Hessman, F. V. 2017, AJ, 153, 77
Correia, A. C. M. 2014, A&A, 570, L5
Cortés-Contreras, M., Béjar, V. J. S., Caballero, J. A., et al. 2017, A&A, 597, A47
Crida, A., Ligi, R., Dorn, C., Borsa, F., & Lebreton, Y. 2018, RNAAS, 2, 172
Crossfield, I. J. M., Malik, M., Hill, M. L., et al. 2022, ApJL, 937, L17
Cuntz, M., Saar, S. H., & Musielak, Z. E. 2000, ApJ, 533, L151
Dai, F., Masuda, K., Winn, J. N., & Zeng, L. 2019, ApJ, 883, 79
Dai, F., Howard, A. W., Batalha, N. M., et al. 2021, AJ, 162, 62
Demory, B.-O., Gillon, M., de Wit, J., et al. 2016, Natur, 532, 207
Essack, Z., Seager, S., & Pajusalu, M. 2020, ApJ, 898, 160
Foreman-Mackey, D., Hogg, D. W., Lang, D., & Goodman, J. 2013, PASP, 125, 306
Gagné, J., Mamajek, E. E., Malo, L., et al. 2018, ApJ, 856, 23
Gaia Collaboration, Brown, A. G. A., Vallenari, A., et al. 2018, arXiv:1804.09365
Gaia Collaboration, Vallenari, A., Brown, A. G. A., et al. 2022, arXiv:2208.00211
Gaidos, E., Claytor, Z., Dungee, R., Ali, A., & Feiden, G. A. 2023, MNRAS, 520, 5283
Gaidos, E., Mann, A. W., Lépine, S., et al. 2014, MNRAS, 443, 2561
Galarza, J. Y., López-Valdivia, R., Meléndez, J., & Lorenzo-Oliveira, D. 2021, ApJ, 922, 129
Gardner, J. P., Mather, J. C., Clampin, M., et al. 2006, SSRv, 123, 485
Gibson, S. R., Howard, A. W., Marcy, G. W., et al. 2016, Proc. SPIE, 9908, 990870
Gibson, S. R., Howard, A. W., Roy, A., et al. 2018, Proc. SPIE, 10702, 107025X
Gibson, S. R., Howard, A. W., Rider, K., et al. 2020, Proc. SPIE, 11447, 1144742
Ginzburg, S., Schlichting, H. E., & Sari, R. 2018, MNRAS, 476, 759
Gliese, W., & Jahreiß, H. 1991, in Preliminary Version of the Third Catalogue of Nearby Stars, On: The Astronomical Data Center CD-ROM: Selected Astronomical Catalogs, ed. L. E. Brotzmann & S. E. Gesser, Vol. I (Washington, DC: NASA)
Goldreich, P., & Soter, S. 1966, Icar, 5, 375
Grunblatt, S. K., Howard, A. W., & Haywood, R. D. 2015, ApJ, 808, 127
Hachisu, I. 1986a, ApJS, 61, 479
Hachisu, I. 1986b, ApJS, 62, 461
Han, T., & Brandt, T. D. 2023, AJ, 165, 71
Handley, L. B., Petigura, E. A., Mišić, V. V., Lubin, J., & Isaacson, H. 2024, AJ, 167, 122
Hansen, B. M. S., & Murray, N. 2013, ApJ, 775, 53
Hatzes, A. P., Fridlund, M., Nachmani, G., et al. 2011, ApJ, 743, 75
Hayward, T. L., Brandl, B., Pirger, B., et al. 2001, PASP, 113, 105
Haywood, R. D., Collier Cameron, A., Queloz, D., et al. 2014, MNRAS, 443, 2517
Hellard, H., Csizmadia, S., Padovan, S., et al. 2019, ApJ, 878, 119
Howard, A. W., Sanchis-Ojeda, R., Marcy, G. W., et al. 2013, Natur, 503, 381
Hu, R., Ehlmann, B. L., & Seager, S. 2012, ApJ, 752, 7
Huber, D., Zinn, J., Bojsen-Hansen, M., et al. 2017, ApJ, 844, 102
Jenkins, J. M., Twicken, J. D., McCauliff, S., et al. 2016a, Proc. SPIE, 9913, 99133E
Jenkins, J. M., Twicken, J. D., McCauliff, S., et al. 2016b, Proc. SPIE, 9913, 99133E

Jia, S., & Spruit, H. C. 2017, MNRAS, 465, 149
Kellermann, C., Becker, A., & Redmer, R. 2018, A&A, 615, A39
Kempton, E. M. R., Bean, J. L., Louie, D. R., et al. 2018, PASP, 130, 114401
Kipping, D. M. 2013, MNRAS, 435, 2152
Kite, E. S., Fegley, B., Jr, Schaefer, L., & Gaidos, E. 2016, ApJ, 828, 80
Koll, D. D. B., & Abbot, D. S. 2015, ApJ, 802, 21
Kovács, G., Zucker, S., & Mazeh, T. 2002, A&A, 391, 369
Krásná, H., Böhm, J., & Schuh, H. 2013, JGeo, 70, 21
Kreidberg, L. 2015, PASP, 127, 1161
Kreidberg, L., Koll, D. D. B., Morley, C., et al. 2019a, Natur, 573, 87
Kreidberg, L., Koll, D. D. B., Morley, C., et al. 2019b, Natur, 573, 87
Laine, R. O., & Lin, D. N. C. 2012, ApJ, 745, 2
Lam, K. W. F., Csizmadia, S., Astudillo-Defru, N., et al. 2021, Sci, 374, 1271
Lambeck, K. 1980, The Earth's Variable Rotation: Geophysical Causes and Consequences, Cambridge Monographs on Mechanics (Cambridge: Cambridge Univ. Press)
Leconte, J., Lai, D., & Chabrier, G. 2011, A&A, 528, A41
Lee, E. J., & Chiang, E. 2017, ApJ, 842, 40
Lépine, S., Hilton, E. J., Mann, A. W., et al. 2013, AJ, 145, 102
Li, S.-L., Miller, N., Lin, D. N. C., & Fortney, J. J. 2010, Natur, 463, 1054
Liu, F., Ting, Y.-S., Yong, D., et al. 2024, Natur, 627, 501
Lomb, N. R. 1976, Ap&SS, 39, 447
Lopez, E. D. 2017, MNRAS, 472, 245
Love, A. E. H. 1944, A Treatise on the Mathematical Theory of Elasticity (4th edn.; New York: Dover Publications), http://www.worldcat.org/isbn/0486601749
Lucy, L. B., & Sweeney, M. A. 1971, AJ, 76, 544
Lundkvist, M. S., Kjeldsen, H., Albrecht, S., et al. 2016, NatCo, 7, 11201
Mann, A. W., Dupuy, T., Kraus, A. L., et al. 2019, ApJ, 871, 63
Marfil, E., Tabernero, H. M., Montes, D., et al. 2021, A&A, 656, A162
MAST 2021, TESS Light Curves—All Sectors, STScI/MAST,
McQuillan, A., Mazeh, T., & Aigrain, S. 2014, ApJS, 211, 24
Melrose, D. B., & Dulk, G. A. 1982, ApJ, 259, 844
Morris, R. L., Twicken, J. D., Smith, J. C., et al. 2020, Kepler Science Document KSCI-19081-003
Morris, S. L. 1985, ApJ, 295, 143
Morton, T. D., 2015 Isochrones: Stellar Model Grid Package, Astrophysics Source Code Library, ascl:1503.010
Moutou, C., Donati, J. F., Lin, D., Laine, R. O., & Hatzes, A. 2016, MNRAS, 459, 1993
Moutou, C., Hébrard, E. M., Morin, J., et al. 2017, MNRAS, 472, 4563
Murray, C. D., & Dermott, S. F. 1999, Solar System Dynamics (Cambridge: Cambridge Univ. Press)
Nagar, T., Spina, L., & Karakas, A. I. 2019, arXiv:1911.09861
Nagel, E., Czesla, S., Kaminski, A., et al. 2023, A&A, 680, A73
Nan, R., Li, D., Jin, C., et al. 2011, IJMPD, 20, 989
Narita, N., Fukui, A., Kusakabe, N., et al. 2019, JATIS, 5, 015001
Narita, N., Fukui, A., Yamamuro, T., et al. 2020, Proc. SPIE, 11447, 114475K
Newville, M., Stensitzki, T., Allen, D. B., & Ingargiola, A. 2014, LMFIT: Non-Linear Least-Square Minimization and Curve-Fitting for Python, v0.8.0, Zenodo, doi:10.5281/zenodo.11813
NExScI 2022, Exoplanet Follow-up Observing Program Web Service, IPAC, doi:10.26134/EXOFOP5
Ofir, A. 2014, A&A, 561, A138
Ofir, A., & Dreizler, S. 2013, A&A, 555, A58
Ogilvie, G. I. 2014, ARA&A, 52, 171
Ogilvie, G. I., & Lin, D. N. C. 2007, ApJ, 661, 1180
Oh, S., Price-Whelan, A. M., Brewer, J. M., et al. 2018, ApJ, 854, 138
Owen, J. E., & Wu, Y. 2017, ApJ, 847, 29
Peale, S. J., Cassen, P., & Reynolds, R. T. 1979, Sci, 203, 892
Penev, K., Bouma, L. G., Winn, J. N., & Hartman, J. D. 2018, AJ, 155, 165
Perez-Becker, D., & Chiang, E. 2013, MNRAS, 433, 2294

Petigura, E. A. 2015, PhD thesis, University of California, Berkeley
Petrovich, C., Deibert, E., & Wu, Y. 2019, AJ, 157, 180
Plotnykov, M., & Valencia, D. 2020, MNRAS, 499, 932
Plotnykov, M., & Valencia, D. 2024, MNRAS, 530, 3488
Pollacco, D. L., Skillen, I., Collier Cameron, A., et al. 2006, PASP, 118, 1407
Price, E. M., & Rogers, L. A. 2020, ApJ, 894, 8
Pu, B., & Lai, D. 2019, MNRAS, 488, 3568
Quirrenbach, A., Amado, P. J., Caballero, J. A., et al. 2014, Proc. SPIE, 9147, 91471F
Quirrenbach, A., CARMENES Consortium, Amado, P. J., et al. 2020, Proc. SPIE, 11447, 114473C
Ramírez, I., Khanal, S., Aleo, P., et al. 2015, ApJ, 808, 13
Rappaport, S., Barclay, T., DeVore, J., et al. 2014, ApJ, 784, 40
Rappaport, S., Sanchis-Ojeda, R., Rogers, L. A., Levine, A., & Winn, J. N. 2013, ApJL, 773, L15
Rappaport, S., Levine, A., Chiang, E., et al. 2012, ApJ, 752, 1
Ricker, G. R., Winn, J. N., Vanderspek, R., et al. 2015, JATIS, 1, 014003
Ross, C. 1999, Mechanics of Solids, Horwood Engineering Science Series (Amsterdam: Elsevier Science), https://books.google.com/books?id=H_5zV2twBtwC
Rubenzahl, R. A., Halverson, S., Walawender, J., et al. 2023, PASP, 135, 125002
Saar, S. H., & Linsky, J. L. 1985, ApJL, 299, L47
Saiang, C., & Miskovsky, K. 2011, in ISRM Congress 12, Effect of Heat on the Mechanical Properties of Selected Rock Types–A Laboratory Study (Beijing: ISRM)
Sanchis-Ojeda, R., Rappaport, S., Winn, J. N., et al. 2014, ApJ, 787, 47
Sanchis-Ojeda, R., Rappaport, S., Winn, J. N., et al. 2013, ApJ, 774, 54
Sanchis-Ojeda, R., Rappaport, S., Pallè, E., et al. 2015, ApJ, 812, 112
Scargle, J. D. 1982, ApJ, 263, 835
Schlaufman, K. C., Lin, D. N. C., & Ida, S. 2010, ApJL, 724, L53
Schweitzer, A., Passegger, V. M., Cifuentes, C., et al. 2019, A&A, 625, A68
Seager, S., & Mallén-Ornelas, G. 2003, ApJ, 585, 1038
Smith, A. M. S., Cabrera, J., Csizmadia, S., et al. 2018, MNRAS, 474, 5523
Spina, L., Sharma, P., Meléndez, J., et al. 2021, NatAs, 5, 1163
Stumpe, M. C., Smith, J. C., Catanzarite, J. H., et al. 2014, PASP, 126, 100
Tabernero, H. M., Marfil, E., Montes, D., & González Hernández, J. I. 2022, A&A, 657, A66
Takahashi, E. 1986, JGRB, 91, 9367
Tayar, J., Claytor, Z. R., Huber, D., & van Saders, J. 2022, ApJ, 927, 31
Trifonov, T., Tal-Or, L., Zechmeister, M., et al. 2020, A&A, 636, A74
Twicken, J. D., Clarke, B. D., Bryson, S. T., et al. 2010, Proc. SPIE, 7740, 774023
Valencia, D., Sasselov, D. D., & O'Connell, R. J. 2007, ApJ, 656, 545
van Haarlem, M. P., Wise, M. W., Gunst, A. W., et al. 2013, A&A, 556, A2
van Lieshout, R., & Rappaport, S. A. 2018, in Handbook of Exoplanets, ed. H. J. Deeg & J. A. Belmonte (Berlin: Springer), 15
Vanderspek, R., Huang, C. X., Vanderburg, A., et al. 2019, ApJ, 871, L24
Vogt, S. S., Radovan, M., Kibrick, R., et al. 2014, PASP, 126, 359
Wei, X., & Lin, D. N. C. 2024, ApJ, 965, 88
Weinberg, N. N., Sun, M., Arras, P., & Essick, R. 2017, ApJL, 849, L11
Whittaker, E. A., Malik, M., Ih, J., et al. 2022, AJ, 164, 258
Winn, J. N., Sanchis-Ojeda, R., & Rappaport, S. 2018, arXiv:1803.03303
Winn, J. N., Matthews, J. M., Dawson, R. I., et al. 2011, ApJL, 737, L18
Yee, S. W., Petigura, E. A., & von Braun, K. 2017, ApJ, 836, 77
Zarka, P. 1998, JGR, 103, 20159
Zechmeister, M., Reiners, A., Amado, P. J., et al. 2018, A&A, 609, A12
Zeng, L., Sasselov, D. D., & Jacobsen, S. B. 2016, ApJ, 819, 127
Zeng, L., Jacobsen, S. B., Sasselov, D. D., et al. 2019, PNAS, 116, 9723
Zhang, M., Hu, R., Inglis, J., et al. 2024, ApJL, 961, L44
Zhang, Y., Liu, S.-F., & Lin, D. N. C. 2021, ApJ, 915, 91